Journal of Structural Geology 184 (2024) 105155

Contents lists available at ScienceDirect

Journal of Structural Geology

journal homepage: www.elsevier.com/locate/jsg

Multiscale fracture, physical and mechanical properties of stromboli volcano (Italy) edifice

T. Alcock [a], S. Vinciguerra [a,*], P.M. Benson [b], D. Bullen [b]

[a] Department of Earth Sciences, University of Turin, Italy
[b] Rock Mechanics Laboratory, School of Earth and Environmental Sciences University of Portsmouth, England, UK

ARTICLE INFO

Keywords:
Deformation mechanisms
Structural geology
Rock rheology
Tectonics
3D virtual outcrop
Geo-models
Microtectonics

ABSTRACT

The physical, mechanical and fracture properties at Stromboli volcano have been integrated at multiple scales to understand whether the interplay between a presumed NE/SW rift zone and the Sciara del Fuoco (SDF) depression has resulted in a zone of weakness able to promote fracturing prone to flank instability. Multiscale fracture quantification by imaging via FracPaQ toolbox both fractures and sample scale fractures has been integrated with rock physics and rock mechanics experiments on cm-scale samples belonging to the Paleostromboli, Vancori, Neostromboli, Pizzo and Present Deposit volcanic cycles that have been taken from within and outside the rift zone. The structural changes to the edifice have been quantitively assessed by mapping at different scale fracture properties such density and orientation within and outside the rift zone allowing to identify the potential damaged zones that could reduce the edifice strength.

Results indicate that basalt textures, microfracture density, porosity, chemical zoning and preferential alignments, despite lithologically dependent, can be related to the NE/SW zone of weakness at the regional scale and to collapsed volumes that have been subject to continuous intrusive activity. Numerical inversion models have been performed to cross correlate fracture density in the basalts at multiple scales.

A link between microfracture density and seismic velocities has been also established via numerical modelling, allowing to interpret in terms of degree of fracturing the results of seismic tomographies at the field scale, providing a novel method to image crack damage evolution within the inner structure of the volcano edifice.

1. Introduction

Volcanoes are active geologically systems in which their volcano-tectonic processes can induce edifice instability resulting in their collapse (Acocella and Tibaldi, 2005). Monitoring and quantifying the effects of volcanic instability is important for understanding the morphological evolution of a volcanic system. Multiple studies have been conducted on edifices around the world to assess their structural vulnerability to volcano-tectonic processes such as ground motion initiated via earthquakes or through over loading of volcanic flanks (Swanson et al., 1976; Voight and Elsworth, 1997). Mass failure along a volcanic flank can commonly be attributed to dike intrusions disrupting the equilibrium of a slope (Reid et al., 2010). Over time repeated inflation-deflation and buttressing from subsurface magmatic activity can ultimately result in morphological changes to a volcanic edifice (Tibaldi et al., 2009). Edifice collapse may be followed by phases of rapid construction as well as changes in the composition of erupted lavas associated with decompression changes influencing magma chamber processes (Hildenbrand et al., 2004; Pinel and Jaupart, 2005; Hora et al., 2007; Manconi et al., 2009). With this understanding, analysing the physical state of the volcanic edifice in terms of crack damage can help to identify and discriminate the mechanisms controlling edifice instability at different scales.

Satellite observation and field structural surveys have been performed to analyse the state of the volcano edifice. Through mapping and modelling the topological features of a volcano edifice one can gauge how morphological changes may evolve with respect eruptive episodes. High resolution satellite data has been incorporated into multiple studies to provide quantitative assessments on the distribution of volcano-tectonic structures and main lineaments on the volcano edifice. Remote sensing data has been used in volcano-tectonic environments such as at Mt Etna (Italy), Stromboli (Italy) and Shiveluch (Russia) to monitor the changing morphology of the edifices to determine how eruptive events impact on the formation surface features

* Corresponding author.
E-mail address: sergiocarmelo.vinciguerra@unito.it (S. Vinciguerra).

https://doi.org/10.1016/j.jsg.2024.105155
Received 6 September 2023; Received in revised form 2 May 2024; Accepted 9 May 2024
Available online 10 May 2024

(Palaseanu-Lovejoy et al., 2019; Di Traglia et al., 2021; Shevchenko et al., 2021). At Shiveluch, a combination of high-resolution images captured from the Pleiades and radar TanDEM-X satellites was used to assess the 2019 dome collapse. Satellite observation helped to quantitively determine structural changes to the edifice, whilst also providing a better understanding of the formation of lineaments and on the stress regime acting on the volcano (Shevchenko et al., 2021).

Experimental Rock Deformation can provide physical support into the coupled relationship between physical, mechanical and microstructural properties of rocks involved in the deforming edifice. The behaviour of volcanic rock under varying effective pressure has been explored by multiple authors, whom have directly linked the effect of varying porosity and micro fracturing to the mechanical behaviour (Apuani et al., 2005a, 2005b; Heap et al., 2014; Zhu et al., 2016; Heap and Violay, 2021). The increase in porosity has a direct influence of the decrease of strength and Young's Modulus, although Poisson's Ratio for volcanic rocks do not evolve systematically as a function of porosity (Heap et al., 2020b). Heap and Violay (2021) have presented a comprehensive review of how porosity influences the uniaxial compressive strength (UCS) of volcanic rocks and have further explored how other microstructural parameters such as pore size and shape have a direct impact on the failure characteristics of rocks under pressure. Mineral and textural alteration has also been known to influence the formation of additional fracturing in volcanic rocks (del Potro and Hürlimann, 2009; Pola et al., 2014; Heap et al., 2021a). Evidence has been presented suggesting that compressive strength of hydrothermally altered volcanic rocks can vary with degrees of alteration and decreasing or increasing the strength of volcanic rock, because of the change of microfracture interconnectivity and pore space distribution (Heap et al., 2021b). Fracture and void characterization within rocks are important for understanding how stress is distributed throughout a sample and what effect this could have on the failure strength of a rock and thus for the modelling of edifice collapse mechanisms.

Assessing the physical and mechanical properties of rock samples are thus key for quantifying the failure mechanisms that can drive flank instability and are important for understanding the continuous evolution of an edifice. Here we present a multiscale interpretation of fracture and microfracture properties of Stromboli basalts to quantify crack damage and identify potential weaknesses that can promote edifice instability.

1.1. Stromboli volcanic edifice, fracture analysis and sample selection

A stratigraphic framework for the volcano has been established by connecting units that have been bounded by unconformities with Epochs defined by volcanic activity (Francalanci et al., 2013; Lucchi, 2019). The six successive eruptive Epochs, Paleostromboli I – III (Epoch 1–3), Lower and Upper Vancori (Epoch 4), Neostromboli (Epoch 5); Recent Sciara, Pizzo and Present Deposits (Epoch 6) have been described thoroughly in (Francalanci et al., 2013). The Epochs have been characterised by the location of their volcanic centres as well as their chemical composition. The Epochs have been separated by periods of major erosional stages such as caldera collapses and lateral failures that have shaped the edifice. Subdivisions within the Epochs have been arranged into eruptive phases and pulses defined by the volcanic material produced from lava flows, lahars and pyroclastic density currents as well as hydromagmatic activity (Fisher and Schmincke, 1984).

Structural field data collected on Stromboli has revealed a detailed reconstruction of intrusive activity that has taken place during the last 100 ka (Tibaldi, 1996; Corazzato et al., 2008; Tibaldi et al., 2009). The dating of intrusive sheets has revealed the influence of a regional tectonic stress with a northwest southeast σ_3 that has governed the location and direction of magma pathways. A NE–SW trending rift zone has developed passing across the centre of the summit consequently resulting in preferential orientation N-NE strike of intrusive events that have become more vertical and abundant toward the rift axis (Tibaldi, 1996, 2003; Corazzato et al., 2008; Tibaldi et al., 2014; Patanè et al., 2017). Furthermore, structural data has revealed that in the last 13 ka magma sheets have intruded in horseshoe shape along the NW of the edifice where 4 major flank collapses have taken place leading to the formation of the Sciara del Fuoco (SDF) (Apuani et al., 2005a, 2005b; Apuani and Corazzato, 2009; Francalanci et al., 2013). The SDF has remained unstable due to the influence of lateral creep which as provided space along the slope boundary for the thinner intrusions to be emplaced. The consequence of the seaward displacement of the SDF is an eventual sector collapse at the shoulders of the slope (Apuani et al., 2005a; Apuani and Corazzato, 2009; Francalanci et al., 2013).

Previous studies have also identified evidence of alteration of basaltic rocks that has taken place at Stromboli (del Moro et al., 2011; Finizola et al., 2003; Francalanci et al., 2013). At a mesoscale, Finizola et al. (2003) have examined the shallow hydrothermal activity at Stromboli in order to determine the structural framework of the summit area. Their work assessed the rise of hot fluid by monitoring soil self-potential, temperature and gas anomalies. The results of the study highlighted that the shallow fluid circulation has utilized fault and fracture networks beneath the surface then accumulated beneath the summit to form a hydrothermal zone. Hydrothermal alteration of material has been studied by del Moro et al. (2011), at a microscale to determine the mineralogical features of ejecta emitted during paroxysmal explosions at Stromboli volcano. They have identified that the circulation of acidic fluids has led to Stromboli rocks exhibiting argillic and silicic alteration. The authors have identified that phenocrysts of plagioclase and clinopyroxene have not experienced a high degree of alteration however, olivine was observed to have oxidised to hematite. Compositional changes, as a result of magma mixing and mush cannibalism, are reflected in geochemical and textural analysis. Studies have found that at Stromboli volcano, plagioclase, olivine, pyroxenes crystals have been subjected to reabsorption as well as feature chemical zoning and oxidation (Petrone et al., 2006, 2022; Rossi et al., 2019; Di Stefano et al., 2020).

2. Methodology

2.1. Satellite fracture analysis and sample selection

A 0.5 m Pleiades tri stereo satellite image was used to generate a digital elevation model (DEM) of the island to assess the distribution of fracture networks across the island. Structural features associated with episodes of intrusions and tectonic lineaments were recorded and classified using both aerial and field photographs as well as previous structural surveys (Tibaldi et al., 2003; Tibaldi and Corazzato, 2009). Fracture maps of the island were manually drawn and subsequently processed using the fracture mapping MatLab toolbox FracPaQ (Healy et al., 2017). This toolbox was used to quantify the fracture density and preferential orientations from the satellite data, allowing these to be linked to the rift processes that have taken place during the life span of the volcano. The code employs the Mauldon method to determine the length of fracture segments, their strike and density within a selected area (Mauldon et al., 2001). Fracture density, defined as the number fractures per unit area, was determined by calculating the number of intersections between fracture outlines in a circular radius, and the number of trace endpoints in a circular window respectively. Fracture trace lengths, defined as the average length of fractures from each circular window, were also calculated in each image analysis area. FracPaQ was used to create a comparative study of fracture segments from extrusive locations and overlay these onto the structural features in and around the SDF and NE-SW trending rift zone. These 3 areas were of particular interest due to their influence on the structural and morphological history of the edifice. Previous structural investigations, such as have identified areas where extrusive activity has taken place and have defined the outlines of the SDF and the NE/SW trending rift zone the width of which has been defined by the Nel Cannestra and

Vallonazzo extrusive fissures (Tibaldi, 2003; Tibaldi et al., 2003, 2009). By examining these areas, a comparative study can be performed to quantify and cross examine volcano-tectonic fracturing across the volcano.

During fieldwork, careful consideration was taken to ensure that the samples taken from the edifice were representative of temporal evolution that has taken place on the island as described in Francalanci et al., (2013). One block sample was taken from each sample site (Fig. 1) around the edifice to gauge an understanding of the different physical properties of lithological units with respect to their age (Table 1) and location with respect to the Sciara Del Fuoco and the inferred Rift Zone. Vallone del Monaco and Malpasso (Paleostromboli I) basalts are members of the oldest eruptive phase (Epoch 1) and were taken from outside of the proposed rift zone. In contrast to the Vancori, Le Roccette, Filo di Fuoco taken close to the summit of the caldera, in the centre of the rift zone, yet belonged to Epoch 4, 5 and 6 respectively (Vancori, Neostromboli and Present Deposits). Basalts were selected from the edge of the rift zone. San Vincenzo (Neostromboli, Epoch 5) and San Bartolo (Pizzo, Epoch 6) basalts were taken from North and North Eastern edges of the rift zone respectively, whereas Vigna Vecchia (Neostromboli, Epoch 5) basalt was taken from the southern centre of the rift zone. Serro Adorno, Semaforo Labronzo and Ginostra basalts (Neostromboli, Epoch 5) were selected due to their northern and western positions outside of the rift zone.

2.2. Laboratory experimental procedure

The outcrops were oriented considering the field strike and dip. The blocks were unoriented and the coring directions were chosen on the shape of the block. Blocks were cored into 20 × 60 mm cylindrical samples and then characterised by porosity and P-wave velocity in dry and wet conditions on five to six core samples. In order to determine the density and porosity, the cores were weighed prior to being placed in a bath to determine the dry mass (M_d). Following this the cores were placed in a bath for 24hrs to allow water to infiltrate into pore spaces. On removal from the bath the cores were reweighed to determine the saturated mass (M_s), then using Eq. (1) the density (ρ_s) of the cores could be calculated.

$$\rho_s = \frac{M_s}{V} \quad (1)$$

Where V, is the volume of the core samples. Then using Eq. (2), the porosity (φ), of the cores could be determined.

Table 1
Samples collected from Stromboli.

Location	Sample	Lithosome	Epoch	Age (Ka)
1	Vallone del Monaco	Paleostromboli 1	1	77
2	Malpasso	Paleostromboli 1	1	83
3i	Serro Adorno	Neostromboli	5	4
3ii	Semaforo Labronzo	Neostromboli	5	4
4	San Vincenzo	Neostromboli	5	12.5
5	Ginostra	Neostromboli	5	13.8
6	Vigna Vecchia	Neostromboli	5	7
7	Le Roccette	Present Day	6	0.8
8	Filo di Fuoco	Neostromboli	5	12.5
9	San Bartolo	Pizzo	6	2.3
10	Vancori	Vancori	4	13

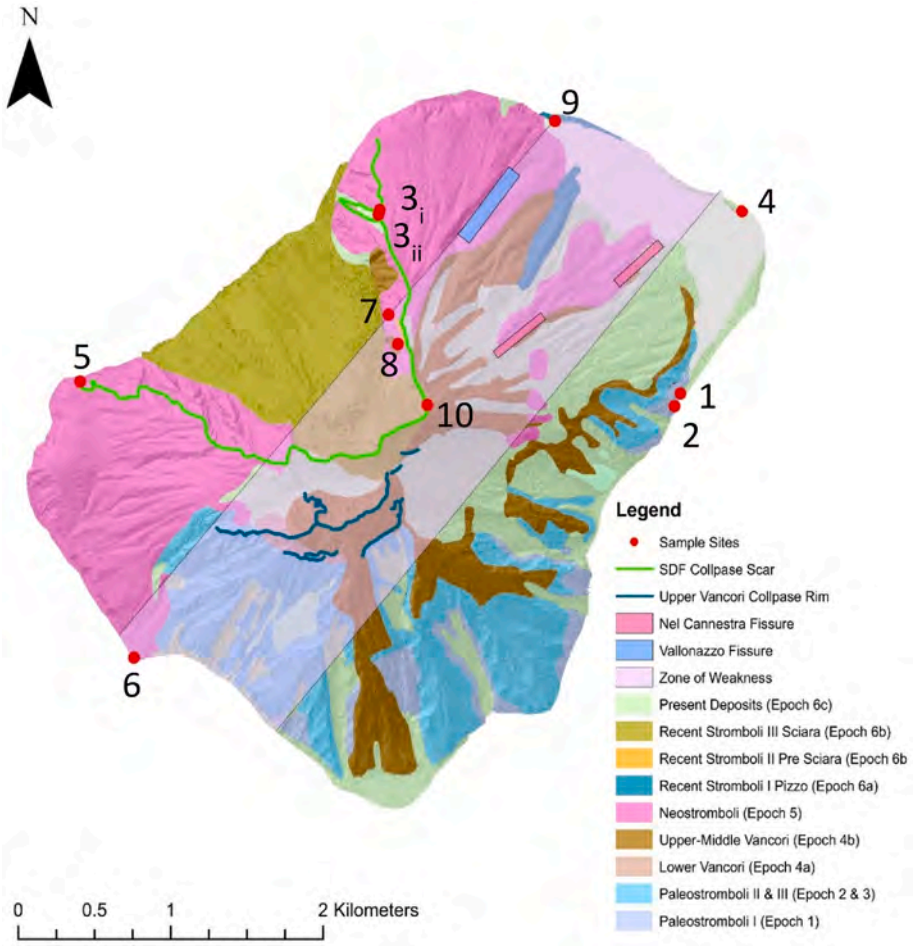

Fig. 1. Geological map of Stromboli highlighting sampling locations.

$$\varphi = \frac{M_s - M_d}{\rho_s} * 100 \quad (2)$$

Using a Wavesurfer 3022 oscilloscope (Fig. 2a) up to six cores for each sample location were measured via the time-of flight method (Simmons and Brace, 1965). The P-wave velocity (Vp) was then calculated (Eq. (3)) using the known distance between the two sensors (d) as well as the average arrival time (t).

$$Vp = \frac{d}{t} \quad (3)$$

UCS tests were performed on five to six cores from each sample location in dry conditions using a 600 kN Instron hydraulic load cell (Fig. 2b) with an internal 200 mm LVDT and a strain gauge used to determine the mechanical characteristics of the basalts such as Young's Modulus and Poisson's ratio from the elastic portion of the experiments. The core samples were put under compression with a strain rate of 1.61 $\times$ 10^{-5} s^{-1} applied in all tests so that an average UCS could be determined for each sample (Fig. 2b). Force and displacement of the hydraulic press were measured internally while a strain gauge was wrapped around the circumference of the core to monitor the outward expansion in order to calculate the Poisson's ratio.

A detailed characterisation of the basalts was done by examining thin section photomicrographs to be then subsequently analysed via the FracPaQ toolbox (Healy et al., 2017). Optical images were taken at 4x on an Olympus microscope to give 5 mm window for analysis. This provided a good resolution to observe fractures and voids within the thin sections. Fracture density and trace length analysis were focused around crystal boundaries, within the groundmass and along pre-existing planes of weakness such as cleavage planes. Fractures were manually drawn taking into consideration their geometry and aspect ratio.

Finally, AMS (anisotropy of magnetic susceptibility) tests were performed to determine the orientation of the magnetic fabric and assess if fracture orientation is influenced from the textural alignment controlled by the lava flow. The dip and strike of selected lava beds were marked on sample blocks that were then cored into 25 mm $\times$ 25 mm core samples. AMS was measured along 3 axes using a kappabridge (Fig. 2c) to determine the principal directions of magnetic fabric lineation (Kmax) and foliation (Kmin). These values were then cross referenced against mean fracture strikes from island scale observations from the selected samples.

3. Petrographic and microfracturing characterisation

Stromboli basalts displayed a porphyritic texture with glomerocrystic aggregates (0.5 mm–3 mm) comprised of plagioclase, olivine and amphibole present in all samples (Fig. 3a–v). Evidence of hydrothermal alteration has been observed in several samples with the presence of microscopic hematite (less than 0.1 mm; Fig. 3e–g & l) concentric zoning (Fig. 3a) and oscillatory zoning (Fig. 3c–g & q) was present in plagioclase feldspars, as well as oxidation (Fig. 3u) observed in augite and biotite around the margins of large elongate to subhedral vesicles (1–2 mm). Microfracturing was also observed along cleavages traces and crystal boundaries of plagioclase, olivine and amphibole crystals in the basalts and emanated outward into the groundmass. Hereafter in detail features for all rock samples investigated are qualitatively described.

3.1. Vallone del Monaco

The Paleostromboli basalt (Fig. 3a, location 1) was highly porphyritic with a fine-crystal to glassy groundmass and a well-defined flow texture displayed by 2 mm in size phenocrysts. The basalt exhibited concentric zoning in plagioclase crystals, Fe-oxides featured along fractures in augite and microfractures were present along plagioclase twinning.

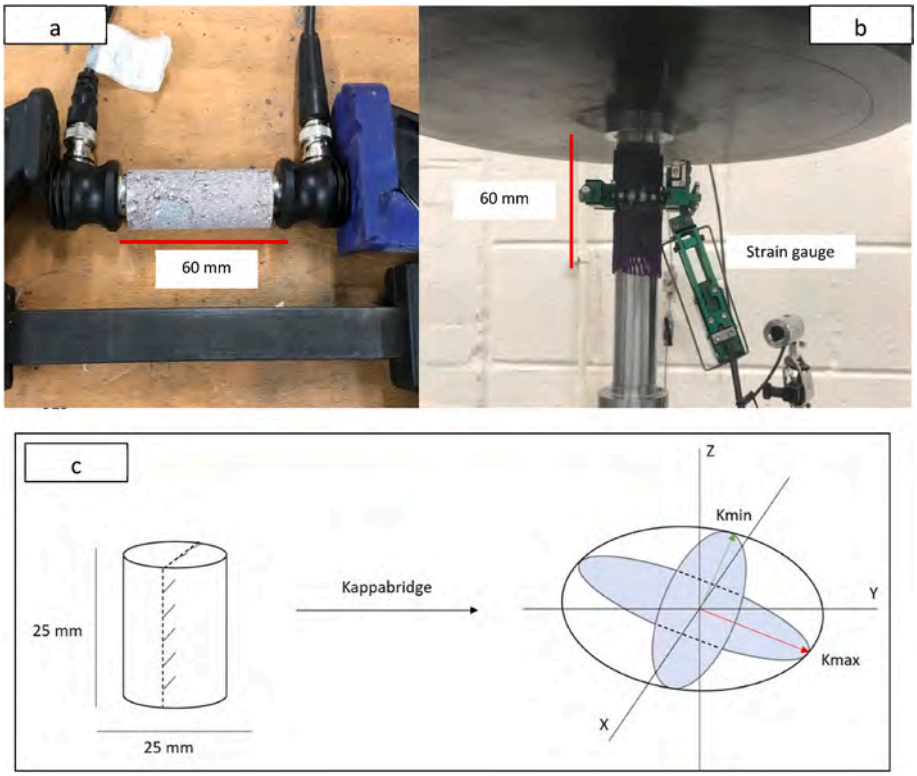

Fig. 2. Example of P-wave velocity measurement using Wavesurfer (a). Example of UCS test using Instron hydraulic press and radial strain gauge to measure elasticity of the basalts (b). Diagram of AMS core and magnetic anisotropy assessment (c) along 3 axes (X, Y, Z) to measure magnetic lineation (Kmax) and foliation (Kmin).

Fig. 3. Thin section (left) and post UCS images of 20 mm diameter cores (right) of sampled basalts: Vallone del Monaco (a & b), Malpasso (c & d), Semaforo Labronzo (e & f), Serro Adorno (g & h), San Vincenzo (i & j), Ginostra (k & l), Vigna Vecchia (m & n), Le Rochette (o & p), Filo de Fuoco (q & r), San Bartolo (s & t) & Vancori (u & v). The thin section images have been captured in cross polarised light with the light modified to examine features within the basalts such as fractures (red), void spaces (green outlines), concentric zoning (cz), oscillatory zoning (oz), oxidation (ox), olivine (Olv), augite (Aug), amphibole (Amp) and plagioclase feldspar (Plg). The thin section image of the Serro Adorno has been captured in plane polarised light in order to better highlight the large void spaces (white). (For interpretation of the references to colour in this figure legend, the reader is referred to the Web version of this article.)

3.2. Malpasso

The Paleostromboli basalt was highly porphyritic with larger elongate vesicles (1 mm) (Fig. 3c, location 2). Fine groundmass pyroxenes had abundant, randomly distributed red oxidised margins. The groundmass was crystalline, with variable crystal size (less than 0.5 mm). Microfractures were randomly orientated in pyroxenes however in plagioclase microfractures mimicked cleavage/twinning in large glomerocrysts, passing from one mineral to another in plagioclase and pyroxene while others terminate or travel along crystal boundaries or propagate to oscillatory zoning patterns that are present in larger plagioclase crystals (1–2 mm).

3.3. Serro Adorno

The Neostromboli basalt was porphyritic with crystals less than 2 mm in size (Fig. 3e, location 3i). Euhedral to subhedral augite crystals occasionally 2.5–3 mm long and fractured along and across cleavage planes. Olivine crystals were smaller (0.75 mm) with irregular fractures that were stained by hematite around the crystal margins. Plagioclase appeared cloudy from abundant groundmass inclusions as well as fragmented and rounded in places. Microfractures in plagioclase mimicked cleavage planes. The groundmass was comprised of fine crystals on a micron scale, including magnetite. The basalt was highly vesicular with sub rounded to rounded 1.4 mm sized vesicles.

3.4. Semaforo Labronzo

The Neostromboli basalt was porphyritic and vesicular with crystals less than 2 mm in size and 1 mm diameter vesicles (Fig. 3g, location 3ii). Olivine crystals were euhedral to subhedral and less than 0.3 mm whereas subhedral augite and plagioclase phenocrysts occurred in similar sizes (2 mm). Plagioclase occurred as blocky laths often well formed with obvious oscillatory zoning. Some were clear while others were cloudy from microscopic groundmass inclusions including hematite and oxidised magnetite. The fine groundmass was dark due to an abundance of microscopic crystals of magnetite, biotite, amphibole as well as oxidation patches. Microfractures in the basalt mimicked and cross cut cleavages in pyroxenes.

3.5. San Vincenzo

The Neostromboli basalt (Fig. 3l, location 4) was porphyritic and comprised of olivine, augite, plagioclase and magnetite phenocrysts.

Olivine phenocrysts were subhedral 1 mm in size with hematite and small plagioclase crystals occurred along fractures and phenocryst margins. Microfractures in olivine phenocrysts mimicked cleavage. Euhedral to subhedral 3 mm long augite phenocrysts were also glomerocrystic and highly fractured along and across with hematite along cleavage planes. Plagioclase was often glomerocrystic, subhedral, occasionally rounded. Plagioclase microfractures occurred along and across cleavage planes. Vesicles in the groundmass varied in size (less than 0.5 mm), roundness and sphericity. Furthermore, the groundmass was abundant in microscopic biotite and hematite and was also composed of plagioclase needles as well as granular magnetite.

3.6. Ginostra

The Neostromboli basalt (Fig. 3k, location 5) was porphyritic with phenocrysts of augite, olivine and plagioclase (from less than 0.5–3 mm) in a fine crystalline groundmass of the same mineral assemblage. The basalt had a well-defined flow texture in various directions. Olivine was colourless and displayed usual irregular microfractures that mimicked cleavage. Augite was glomerocrystic and fractured along and across cleavages. Plagioclase occurred as fresh blocky laths from phenocrysts down to groundmass needles with microfractures that mimicked twinning. Vesicles were subrounded measuring 0.5–1.5 mm. The groundmass varied in crystal size with patches of black, ultra-fine crystalline material (less than 0.1 mm) and abundant in micron-scale brown oxidation patches that occurred around vesicles.

3.7. Vigna Vecchia

The Neostromboli basalt was a porphyritic and glomerocrystic vesicular (Fig. 3m, location 6). Augite, olivine and plagioclase occurred as abundant phenocrysts in the size range less than 0.5–3 mm. Olivine crystals were euhedral with microfractures that crosscut cleavages. Augite and plagioclase occurred as generally euhedral blocky crystals with well-developed microfractures that were developed along cleavages and twins respectively. The groundmass was comprised of very fine crystals; there were sharp and diffuse boundaries with ultra-fine- crystallised to glassy black patches. Vesicles varied in shape and size, from near circular to highly irregular and from less than 0.5 mm–1 mm across.

3.8. Filo di fuoco

The Neostromboli basalt was porphyritic, glomerocrystic and vesicular (Fig. 3o, location 7). The basalt was comprised of less than 0.5 mm–3.5 mm olivine and augite phenocrysts that were fractured along cleavage traces. Fractures within 1 mm plagioclase phenocrysts also occurred along cleavages as well as around concentric zoning. Fractures passed from one crystal to another via the groundmass and between different minerals. Biotite crystals was also observed around the margins of some Fe-stained vesicles.

3.9. Le Roccette

The Neostromboli basalt was a vesicular, highly porphyritic and glomerocrystic with a variably fine crystalline groundmass and flow texture (Fig. 3q, location 8). The basalt was composed of less than 1 mm euhedral olivine crystals as well as augite and plagioclase between 0.5 and 2 mm in size. Microfractures were abundant within the sample and mimic cleavages in augite and oscillatory zoning in plagioclase crystals however were also randomly orientated in pyroxenes.

3.10. San Bartolo

The Neostromboli basalt (Fig. 3s, location 9) was a minimally altered vesicular, highly porphyritic and glomerocrystic olivine basalt with a variably fine, crystalline to glassy groundmass with variable flow texture. The basalt was composed of 1 mm in size subhedral to euhedral olivine and augite crystals as well as 2 mm plagioclase laths. Plagioclase crystals occurred as 2 mm laths with well-developed twins and concentric zoning. Microfracturing in the sample was both random and mimicked cleavages in plagioclase and augite.

3.11. Vancori

The Vancori basalt (Fig. 3u, location 10) was a glomerocrystic basalt with phenocrysts and micro phenocrysts of less than 1 mm–4 mm augite, plagioclase and minor olivine and biotite in a fine crystalline groundmass with a variably orientated flow texture. The sample was defined by its red-brown colour due to the oxidation of fine crystalline groundmass comprised of plagioclase, augite and biotite. Twinning and concentric zoning were well developed in plagioclase whereas olivine phenocrysts were irregular shaped and partially oxidised. Irregular microfractures were present in the basalt but mimicked cleavage and twinning plagioclase and olivine crystals. Microfractures did also emanate from inclusions and others were brown Fe-oxide stained while intergranular fractures occurred along crystal boundaries between crystals.

4. Results

4.1. Island scale fracture analysis

In total, 9503 fractures were related to areas of extrusive activity with an average fracture length of 32 m (Fig. 4). In contrast to the rift zone where 5547 fracture segments were recorded with the average length of fractures being 65 m (Fig. 5a). Similarly, 5551 fracture segments were recorded around the SDF with an average segment length of 20 m (Figs. 5b and 6).

Fracture density was also assessed for each lithosome on the island (Table 2, Fig. 7) showing a linear increase with fracture density and the number of fractures. The Neostromboli lithosome had the greatest number of fractures (7109) and fracture density (1.24E-05 m^{-2}). In contrast to the Pre Sciara lithosome which had the least number of fractures (105) and lowest fracture density (1.81E-07 m^{-2}). Mean fracture strike for all lithosomes was between 024 and 080 (NE/SW).

4.2. Physical and mechanical rock properties

A decrease in the average P-wave velocity in both dry (4.23–3.11 km/s) and saturated conditions (4.88–3.41 km/s) overall is observed (Fig. 8, Table 3). The saturated P-wave velocity is higher in all samples except for Serro Adorno. In dry conditions the highest P-wave velocity values occurred in the older Paleostromboli basalts (4.23 km/s). Neostromboli basalts showed variability in P-wave velocity ranging from 3.02 km/s (San Vincenzo) to 4.18 km/s (Vigna Vecchia). Vancori basalt and Le Roccette basalt (Present Deposits) had a dry P-wave velocity values of 3.70 km/s while San Bartolo from the Pizzo sample had a P-wave velocity of 3.11 Km/s. In saturated conditions, the highest P-wave velocity occurred in Paleostromboli basalts (4.88 and 4.78 km/s). P-wave velocity in saturated Neostromboli basalts ranged from 4.78 km/s (Vigna Vecchia) to 3.41 km/s (Serro Adorno). Vancori, San Bartolo and Le Rochette P-wave velocity values were 4.12 km/s, 3.45 km/s and 3.88 km/s respectively.

A decrease in the average UCS of Stromboli basalts from 92 to 24 MPa with increasing porosity from 2% to 24% is observed as a general pattern (Table 4; Fig. 9). The strongest rocks measured were the older Paleostromboli basalts Vallone del Monaco and Malpasso (92.33 and 81.48 MPa). Neostromboli basalts showed variation with UCS and porosity with the strongest being Filo di Fuoco (69.07 MPa) and the weakest being the Serro Adorno (23.69 MPa). Vancori basalt had a UCS of 32 MPa while basalts from Pizzo and Present Deposits (San Bartolo and Le Rochette) had a UCS of 52.81 MPa and 35.99 MPa respectively.

A decrease in the average Youngs modulus from 11.18 GPa to 4.47

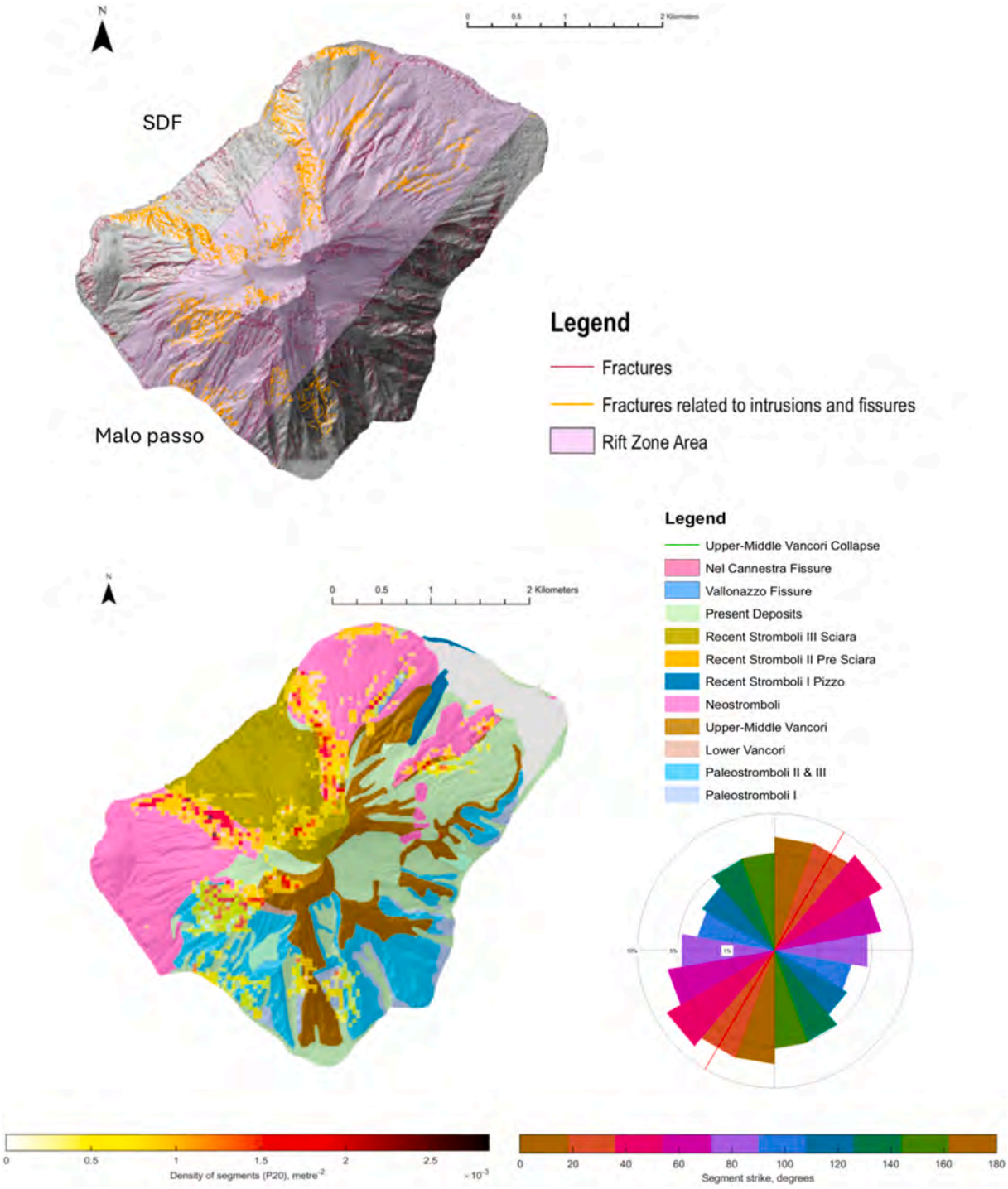

Fig. 4. (a) Fracture map of Stromboli with fractures being separated into those related to intrusions and fissure (orange). (b) Fracture density map of intrusion and fissures. (Right) Rose diagram showing the distribution of strike angles related from intrusion and fissures. (For interpretation of the references to colour in this figure legend, the reader is referred to the Web version of this article.)

GPa with increasing porosity (Fig. 10) is observed. The stiffest Stromboli basalts were the Paleostromboli basalts with Youngs Modulus of 11.18 GPa (Vallone del Monaco) and 10.74 (Malpasso). Neostromboli basalts showed variation in elasticity with the most flexible being Filo de Fuoco (9.21 GPa) and the stiffest rock being from Serro Adorno (4.47 GPa). Vancori basalt had a Youngs Modulus of 7.92 GPa while San Bartolo and Le Rochette (Pizzo and Present Deposits) basalts had a Young's Modulus of 7.48 and 7.11 GPa respectively. The average Poisson's ratio of the basalts showed limited variability with porosity with nearly all basalts having a Poisson's ratio near 0.1 with the exception of Ginostra and Vigna Vecchia basalts that had a Poisson's ratio of 0.16 and the Vancori basalt that exhibited a Poisson's Ratio of 0.06.

4.3. *Microscale fracture analysis*

The Matlab toolbox FracPaQ was used to calculate the variation in the microfracture density (Pc) of Stromboli basalts (Table 5; Fig. 11). The greatest fracture density was recorded in Ginostra basalt (0.012

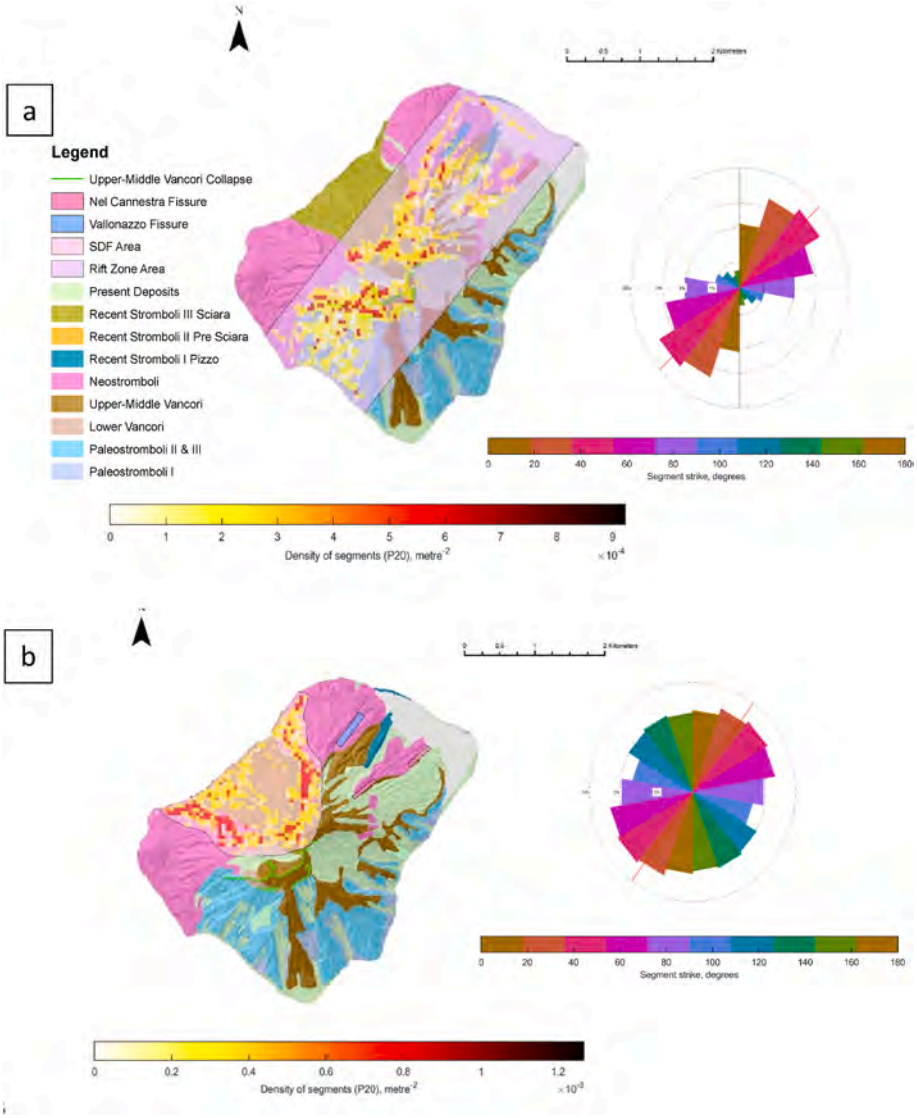

Fig. 5. (a) Fracture density of the NE/SW rift zone across Stromboli. (b) Fracture density of the SDF.

μm^{-2}) whereas Vallone del Monaco basalt displayed the lowest fracture density (0.004 μm^{-2}). There was variation with respect to the number of microfractures in different age. Neostromboli basalt had the highest fracture densities (0.009 μm^{-2} < Pc < 0.011 μm^{-2}) in contrast to Paleostromboli basalts (0.003 μm^{-2} < Pc < 0.007 μm^{-2}), Vancori (0.007 μm^{-2}), Pizzo (0.006 μm^{-2}) and Present Deposits (0.007 μm^{-2}).

There were also variations in the mean number of microfractures with samples taken from different age groups. The number of Paleostromboli basalt (Vallone del Monaco & Malpasso) microfractures was 9423 and 17733. The number of microfractures in Neostromboli basalts ranged from 21814 (Semaforo Labronzo) to 28824 (Ginostra). The number of microfractures in Serro Adorno, San Vincenzo, Vigna Vecchia and Filo de Fuoco was 24808, 23545, 23588, 22706. The number of microfractures in Present Day (Le Rochette), Pizzo (San Bartolo) and Vancori (Vancori) was 18517, 15960 and 17223 respectively.

4.4. Anisotropy of magnetic susceptibility (AMS)

The strike of magnetic fabric lineation's (Kmax) and foliations (Kmin) (Table 6) have been assessed to determine the preferential orientation of structural features on the edifice (Fig. 12). Vallone del Monaco (Paleostromboli 1) Kmax and Kmin were 045 (NW/SE) and 063 (NW/SE) respectively. Vancori basalt Kmax and Kmin was 013 (E/W) and 116 (NW/SE). Serro Adorno Kmax was 098 (N/S) whereas Kmin was 194 (NE/SW). The strike of Neostromboli Kmax ranged from 040 (NE/SW; Vigna Vecchia) to 145 (NW/SE; San Vincenzo). The Kmin strike for the Neostromboli lithosome ranged from 011 (N/S; San Vincenzo) to 194 (S/N; Serro Adorno). The strike of the Kmax and Kmin of the San Bartolo basalt (Pizzo) was 080 (E/W) and 177 (S/N) respectively.

The mean strike was calculated around the sample site location and at a microscale (Table 5, Fig. 12). Island scale fracture strikes (S_i) were NE/SW (020 < S_i < 069) whereas block (S_b) and microscale strike (S_m) orientations were N/SE (002 < S_b < 150) & E/W (070 < S_m < 099) respectively. For Vallone del Monaco (Paleostromboli 1) the mean Island strike was 054 (NW/SE) whereas at a block and microscale the strike was 150 (SE/NW) and 070 (NW/SE). For Vancori basalt the island scale strike was 044 (NW/SE), the block strike was 011 (N/S) and at a microscale the strike was 082(E/W). For Neostromboli basalts the island fracture strike ranged from 036 (NE/SW; Ginostra) to 068 (NE/SW; Semaforo Labronzo). Whereas at a block scale, the fracture strike ranged from 002 (N/S; Vigna Vecchia) to 085 (E/W; San Vincenzo) and at a microscale the fracture strike ranged from 083 (E/W; Ginostra) to 099 (E/W; Serro Adorno). The San Bartolo (Pizzo) basalt had a mean island fracture orientation of 048 (NW/SE), a block fracture orientation of 035 (NE/SW) and a microscale orientation of 088 (E/W).

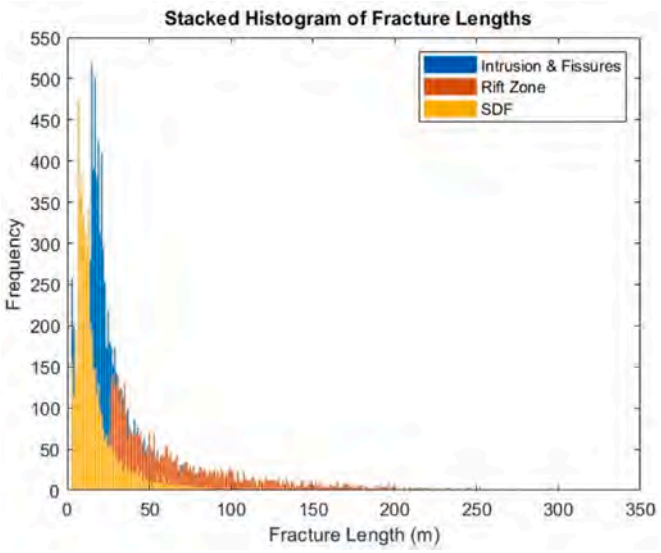

Fig. 6. Stacked histogram of fracture lengths from areas of Intrusions and fissures around the island (blue), the rift zone (orange) and the SDF (yellow) as calculated from FracpaQ. (For interpretation of the references to colour in this figure legend, the reader is referred to the Web version of this article.)

Table 2
Island scale lithosome fracture characteristics.

Lithosome	Number of Fractures	Mean Fracture Density (m^{-2})	±SD	Mean Fracture Strike	±SD
Paleostromboli 1	390	6.78E-07	1.5	024	65
Paleostromboli 2 & 3	4539	7.89E-07	6.8	065	81
Lower Vancori	449	7.81E-07	2.5	101	67
Upper- Middle Vancori	4485	7.80E-07	6.4	035	75
Neostromboli	7109	1.24E-05	9.1	045	72
Pizzo	535	9.30E-07	2.2	117	69
Pre Sciara	105	1.81E-07	1.1	152	75
Sciara	2504	4.48E-06	4.0	095	76
Present Deposits	3441	5.98E-06	4.4	048	71

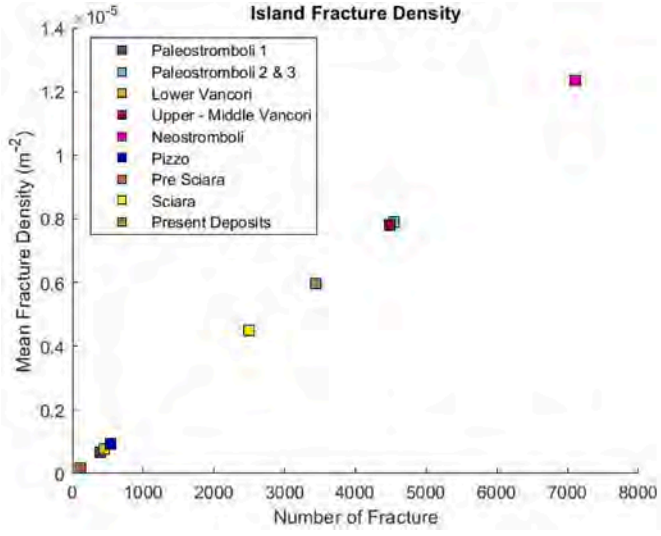

Fig. 7. Scatter plot of number of fractures and fracture density of Stromboli lithosomes.

5. Discussion

The influence on multiscale fracturing as well as the mechanical and physical characteristics of the sampled basalts can be evaluated by assessing the interplay between tectonic activity and the basalt fabrics. At an island scale, localised tectonic activity surrounding the edifice is reflected by fracturing on the surface of the volcano. Terrestrial fracture strike data (Tables 2 and 6) collected from the different lithosomes across the edifice, such as the Paleostromboli 1, the Neostromboli and Upper-Middle Vancori, are closely orientated to the proposed NE/SW zone of weakness (Tibaldi, 1996, 2003; Tibaldi and Corazzato, 2009; Tibaldi et al., 2009). Continuous extensional tectonic activity over the past 100 ka can be considered a driving cause for the parallel orientation of fracturing. The presence of regional NW/SE orientation of least principal stress (σ_3), in conjunction with localised vertical stress (σ_1), from the shallow magma chamber have controlled the rise of successive generations of magma intrusions upward along the proposed NE/SW zone of weakness (Tibaldi, 1996; Tibaldi et al., 2003; Corazzato et al., 2008). The interaction between these stresses can be reflected in the consistent NE/SW orientation of average island scale fractures, as fracture strike around sample sites (Table 6) as well as from their respective lithosomes (Paleostromboli 1, 2 & 3, Upper-Middle Vancori, Neostromboli and in present deposits, Table 2). The effect of volcano-tectonic activity along the zone weakness can be seen around historic episodes of growth and collapse such as the Upper-Middle Vancori and SDF collapse scars as well as along the San Bartolo, Nel Cannestra and Vallonazzo fissures. Surface fracturing can thus be considered a consequence of the interplay between localised intrusive and sector collapse events and give reason to the dispersion of fracture strike observed in Table 2 as well as the increase in the high number of fractures for the Neostromboli and Vancori samples at and island scale (Figs. 7 and 11) (Tibaldi et al., 2009; Di Traglia et al., 2018). Following the collapse of the Upper-Vancori, the geomorphology of the edifice was altered leading to the preferential route for magma in the upper echelons of the edifice to be redirected from along the zone of weakness to parallel with the SDF collapse scarp (Tibaldi, 2003; Tibaldi et al., 2003; White et al., 2011; Intrieri et al., 2013). The intruding magma filled a volume generated around the SDF by gravity and creep pushing the slope outward toward the sea. (Tibaldi et al., 2003, 2009). Trans-tensional and strike-slip fracturing from magma upwelling into the space of the unstable sector can be seen in Figs. 4 and 5 where fracture density was greatest around areas of intrusive activity most notably around the upper margins of the SDF and the summit area of the volcano.

Detailed petrographic examinations have highlighted that that there were also microfracture variations within the crystals as well as the groundmass driven by fast cooling of the lava as it was observed that, overall, the sampled basalts have fine glassy groundmasses with variably flow textures (Fig. 3a–c,e,g,j,k,m,o,q,s) (Vaggelli et al., 2003; Heap et al., 2009, 2010). The AMS of the sampled basalts was compared to island and microscale fracture orientations in order to determine whether multiscale fracturing has been driven from cooling or has tectonically induced. The AMS of Stromboli basalts has shown a varied relationship with island fracture strike data but indicates that the orientation of magnetic fabric matches overall the fracture orientation and thus can influence the fracture behaviour in the rift zone. Within the selected samples taken from around the edifice we observed that in most cases either lineation or foliation was aligned with the mean NE/SW strike (Fig. 12) in fractures across all samples as well as the rift zone (Fig. 5). When assessing AMS and fractures with different zones of interest on the volcano comparisons can be made. The mean Kmax strike of samples collected within the rift zone (Vallone del Monaco, Vigna Vecchia, San Bartolo and Vancori) are orientated on average NW/SE (045, 040, 080 & 013) however the mean Kmin strike of the Vallone del Monaco, Semaforo Labronzo, San Vincenzo, Vigna Vecchia basalts are broadly orientated in line with the rift zone (063, 036, 011 & 082) as

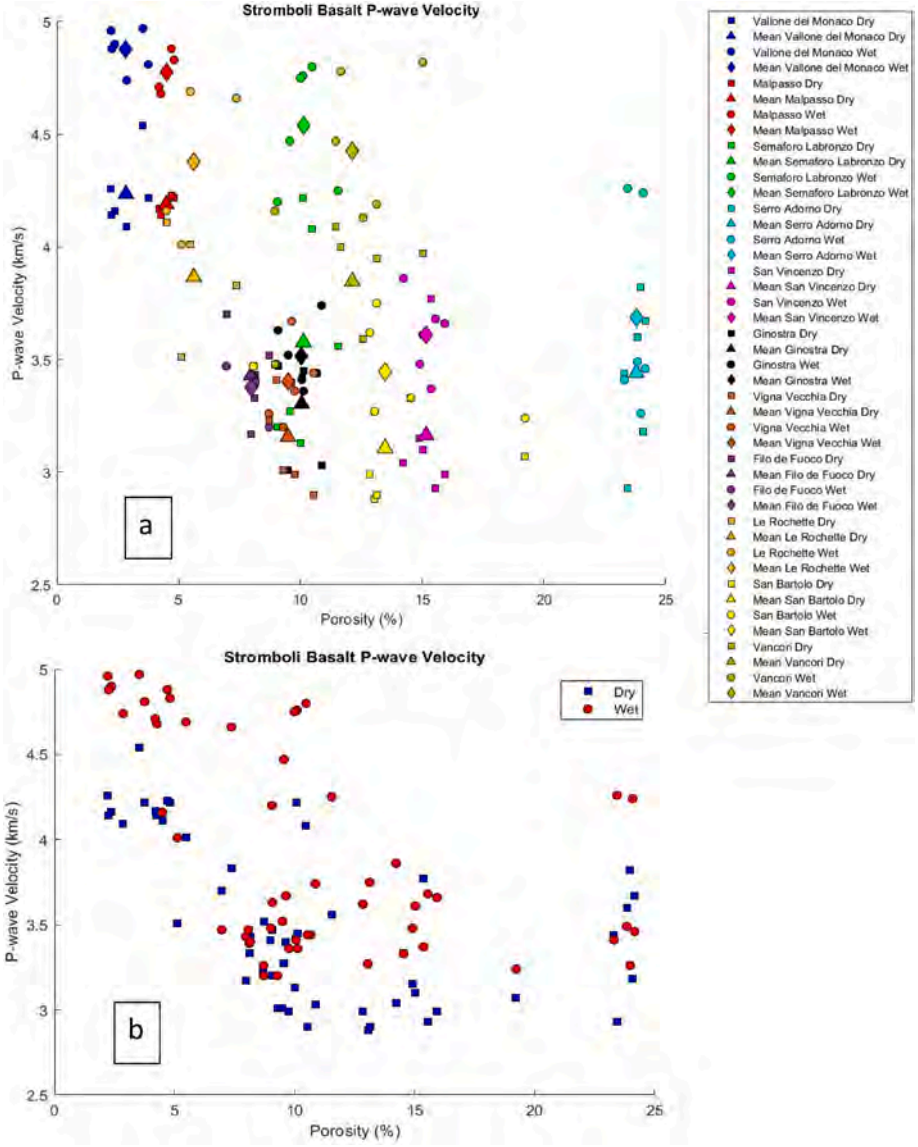

Fig. 8. Scatter plots of P-wave velocities of Stromboli basalts cores (a) in dry and wet conditions (b).

Table 3
Physical and mechanical properties of sampled Stromboli basalts.

Sample	Lithosome	Connected Core Porosity (%)	Dry Core P-wave (Km/s)	±SD	Wet Core P-wave (Km/s)	±SD
Vallone del Monaco	Paleostromboli 1	2.81	4.23	0.05	4.88	0.1
Malpasso	Paleostromboli 1	4.50	4.18	0.02	4.78	0.11
Semaforo Labronzo	Neostromboli	10.13	3.21	0.12	4.36	0.04
Serro Adorna	Neostromboli	23.77	3.57	0.14	3.41	0.03
San Vincenzo	Neostromboli	15.74	3.02	0.02	3.64	0.09
Ginostra	Neostromboli	10.75	3.58	0.07	3.74	0.04
Vigna Vecchia	Neostromboli	9.27	4.18	0.1	4.78	0.04
Filo de Fuoco	Neostromboli	5.62	3.90	0.14	4.44	0.09
Le Rochette	Present Deposits	7.94	3.70	0.15	3.88	0.04
San Bartolo	Pizzo	13.48	3.11	0.14	3.45	0.33
Vancori	Vancori	12.14	3.69	0.15	4.12	0.21

well as their terrestrial fractures which strike NE/SW. Similarly, this observation observed at a block scale where overall the fracture orientation was mainly N/S (006 & 002), for Semaforo Labronzo and Vigna Vecchia basalts, and NE/SW (027, 073, 035 & 011) for Serro Adorno, Ginostra, San Bartolo and Vancori basalts respectively. In several samples the strike of Kmax or Kmin are broadly orientated in the same direction of a secondary strike pattern perpendicular to the orientation of the NE/SW zone of weakness. This can be observed mainly at a microscale (Fig. 12) in Semaforo Labronzo, Serro Adorno, San Vincenzo, Ginostra, San Bartolo and Vancori samples, where either Kmax or Kmin was broadly orientated E/W. This is in a good agreement with the hypothesis of a tensile stress acting across the centre axis of the zone of weakness from a localized σ_1 which has exerted stress onto the upper edifice and aided the development of slope instability (Falsaperla et al.,

Table 4
Mechanical properties of sampled Stromboli basalts.

Sample	Lithosome	UCS (MPa)	±SD	Young's Modulus (GPa)	±SD	Poisson's Ratio	±SD
Vallone del Monaco	Paleostromboli 1	92.33	16.34	11.18	1.75	0.1	0.03
Malpasso	Paleostromboli 1	81.48	15.0	10.74	1.09	0.1	0.03
Semaforo Labronzo	Neostromboli	52.9	12.63	7.59	0.96	0.09	0.04
Serro Adorna	Neostromboli	23.69	2.93	4.47	0.29	0.1	0.03
San Vincenzo	Neostromboli	42.04	4.17	5.73	0.55	0.06	0.02
Ginostra	Neostromboli	49.38	1.73	7.12	0.35	0.16	0.09
Vigna Vecchia	Neostromboli	40.48	3.71	6.21	0.54	0.16	0.04
Filo de Fuoco	Neostromboli	69.07	9.64	9.21	1.08	0.09	0.04
Le Rochette	Present Deposits	52.81	7.86	7.48	0.67	0.09	0.02
San Bartolo	Pizzo	35.99	2.31	7.11	0.26	0.1	0.03
Vancori	Vancori	31.97	6.27	7.92	1.42	0.06	0.03

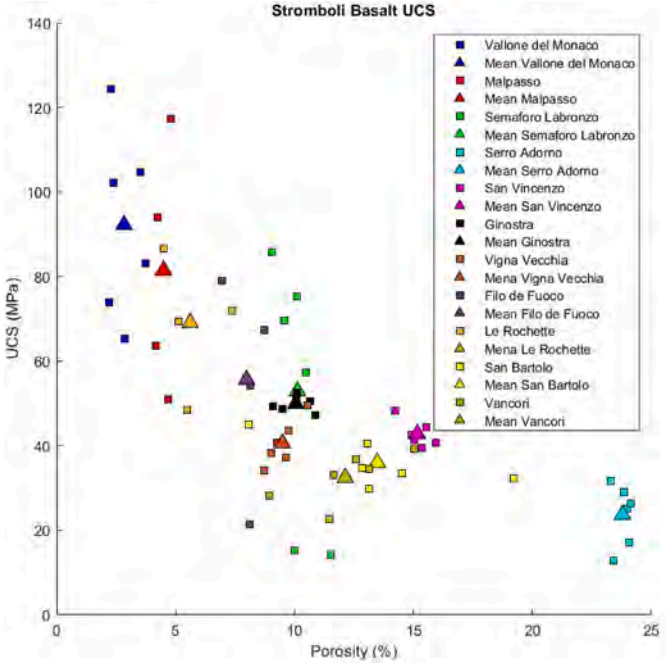

Fig. 9. UCS of Stromboli basalt cores with increasing porosity.

1999; Tibaldi et al., 2003). Multiple studies have identified that the preferential alignment of magnetic material with the local tectonic regime can influence the propagation of fracturing from intrusive activity (Borradaile and Hamilton, 2004; Lu et al., 2008; Bhowmick and Kumar Mondal, 2020). Evidence for this can be present around areas where large scale deformation has occurred on the edifice, such as the Sciara del Fuoco and Upper-Vancori Caldera collapse. Here the lineation and foliation of magnetic fabric has been observed to match the strike of fracturing at the island scale and at the microscale, with the preferential orientation of diking a along the zone of weakness and the SDF. The interplay between magnetic fabric orientation and the regional NE/SW stress regime as well as the localised W-NW/E-SE provides an initial zone of weakness, enhancing generation of multiscale fracturing from which the intrusive sheets can utilise to breach the surface of the edifice. For samples from outside (e.g. Vallone del Monaco) the zone of weakness there is a systematic correspondence between the regional NE/SW tectonic stress and the orientation of fractures as magnetic lineation and foliation were aligned with tectonically induced fracturing as well as at a microscale. Taken all together this indicates that the influence of the regional tectonic stress is not restricted only to the proposed zone of weakness.

Magmas at Stromboli have been recognised as being rich in volatile content, resulting from magma mixing and mush cannibalism, which has resulted in complex mineral and textural compositions of the basalts

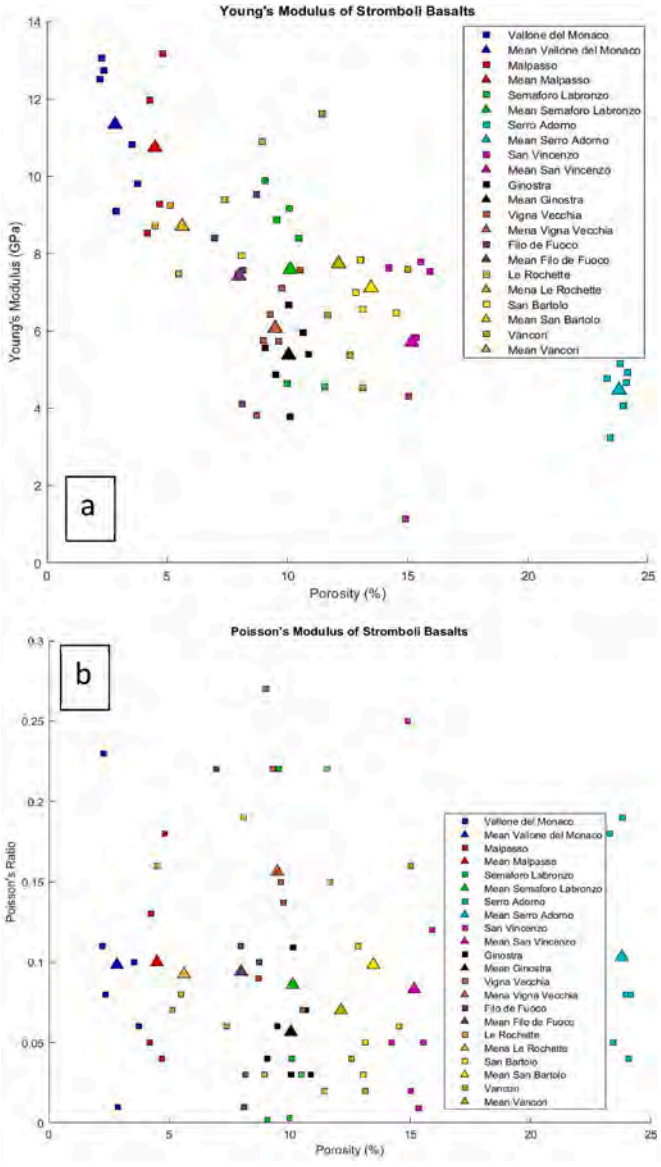

Fig. 10. Young's Modulus (A) and Poisson's (B) ration of Sampled Stromboli basalts.

(Fig. 3a–v) (Bertagnini et al., 2003; Bai et al., 2008; Aiuppa et al., 2010; Edmonds et al., 2010). Composition can influence microfracturing as evidence of asperities, oxidation and zoning were common in basalts from different lithosomes and eruptive Epochs. The result is that, once crystallised, microfracturing has developed along these features

Table 5
Microscale fracture characteristics calculated through FracPaQ.

Sample	Lithosome	Number of Microfractures	±SD	Microfracture density (μm^{-2})	±SD
Vallone del Monaco	Paleostromboli 1	9423	4277	0.004	0.0017
Malpasso	Paleostromboli 1	17733	1893	0.007	0.0008
Serro Adorna	Neostromboli	24808	5536	0.009	0.0022
Semaforo Labronzo	Neostromboli	21814	7434	0.01	0.003
San Vincenzo	Neostromboli	23545	1791	0.009	0.0007
Ginostra	Neostromboli	28824	2775	0.012	0.0011
Vigna Vecchia	Neostromboli	23588	2758	0.009	0.0011
Filo de Fuoco	Neostromboli	22706	1979	0.009	0.0008
Le Rochette	Present Deposits	18517	2130	0.007	0.0009
San Bartolo	Pizzo	15960	1389	0.006	0.0006
Vancori	Vancori	17223	5391	0.007	0.0022

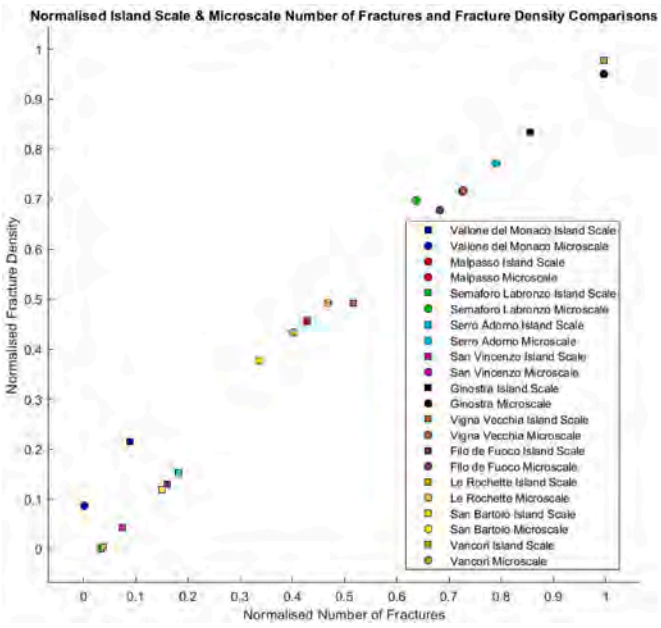

Fig. 11. Normalised number of fractures and fracture density of Stromboli basalts compared at an island scale and microscale.

(Fig. 3a–c,e,g,j,k,m,o,q,s).

Qualitative assessments of the pore geometry of the sampled basalts have identified that the basalts have evolved through time. From the Paleostromboli 1 to the Neostromboli lithosome the pore size and shape in the basalts changed from small (less than 1 mm in diameter) and irregular (Fig. 3a and b) to highly vesicular, regular pores over 1 mm in diameter (Fig. 3c, e, 3g & 3h). Post UCS observations highlighted the influence that pore abundance and distribution on failure modes in the core samples. Samples that consisted of interlocked phenocrysts and low porosities less than 5%, such as Vallone del Monaco (Fig. 3a) and Malpasso (Fig. 3c), had characterised axial splitting failure pattern (Fig. 3b & d). Whereas samples with porosities between 5%–14% showed no clear failure pattern but a coalescence of compression induced fractures were observed to propagate between pores and around phenocrysts (Fig. 3h, j, 3l, 3n, 3p, 3r, 3t & 3v). Highly vesicular basalts such as Serro Adorno (Fig. 3d), with a porosity of 24%, were observed to show a shear failure formed across pore spaces. The effect of pores, microfractures and asperities within the basalts can be quantitively examined by assessing the physical and mechanical properties of the basalts (Fig. 3a–v, 8, 9 & 10). These properties are in agreement with reported studies on the Stromboli edifice as the increasing porosity of the basalts decreased their P-wave velocity, UCS and Young's Modulus (Apuani et al., 2005a, 2005b; Castellano et al., 2008; Patanè et al., 2017). While the Poisson's Ratio was not affected by porosity changes which is in agreement with data collected by Heap et al., (2020). UCS and Young's Modulus data collected in this study is also comparable to mechanical data compiled by Heap et al., (2020) and Heap and Violay (2021). The mechanical properties of Stromboli basalts (Figs. 9 and 10; Table 5) are similar to nearby volcanic systems within the porosity range reported in this study, such as Mt Etna (46 MPa < UCS <123 MPa; 16 GPa < Ɛ < 25 GPa), as well as to afar volcanoes, such as Kilauea, Hawaii (16 MPa < UCS <106 MPa; 5 GPa < Ɛ < 26 GPa) but weaker compared to Turkish Black Sea basalt (47 MPa < UCS <202 MPa) (Karaman and Kesimal, 2015; Zhu et al., 2016; Bubeck et al., 2017).

Older Paleostromboli basalts (Vallone del Monaco and Malpasso) had the greatest P-wave velocity in dry (4.2 Km/s) and wet conditions (4.8 and 4.9 Km/s) as well as the greatest UCS (92.3 and 81.5 MPa) and Young's Moduli (11.2 and 10.7 GPa). This was in contrast to the younger basalts that had varied P-wave velocity in both dry (3.2 < Vp < 4.2 Km/s) and wet conditions (3.4 < Vp < 4.8 Km/s), strength (23.7 < UCS <69.1 MPa) and elasticity (4.5 < Ɛ < 9.2 GPa). The decrease in the physical and mechanical properties with increasing porosity, following the Paleostromboli lithosome, has coincided with the evolution of the Stromboli magma chamber and the Upper-Middle Vancori collapse. As observed in Figs. 8–10, the physical and mechanical properties of basalts vary with respect to different lithosomes with the Neostromboli lithosome showing the most variation. This can be related to the increase in to the K_2O (3.75 wt% < K_2O) and Sr (700 ppm < Sr < 850 ppm) contents as established in Francalanci et al., (2013) (Fig. 13). The evolution of basalt composition and thus differences to physical and mechanical characteristics have been proposed to be generated from a depleted mantle wedge source containing variations in Sr, supercritical liquid and partial melts (Francalanci et al., 2013) . Neostromboli basalts were

Table 6
AMS magnetic lineation and foliation of Stromboli Basalts.

Sample	Lithosome	Kmax Strike	Kmin Strike	Island Fracture Strike	±SD	Block Fracture Strike	±SD	Microfracture Strike	±SD
Vallone del Monaco	Paleostromboli 1	045	063	054	66	150	73	070	78
Serro Adorno	Neostromboli	098	194	020	73	027	77	099	78
Semaforo Labronzo	Neostromboli	143	036	068	52	006	76	090	79
San Vincenzo	Neostromboli	145	011	037	75	085	79	084	78
Ginostra	Neostromboli	138	140	036	76	073	79	083	80
Vigna Vecchia	Neostromboli	040	082	069	78	002	61	088	77
San Bartolo	Pizzo	080	177	048	70	035	75	088	79
Vancori	Vancori	013	116	044	73	011	77	082	78

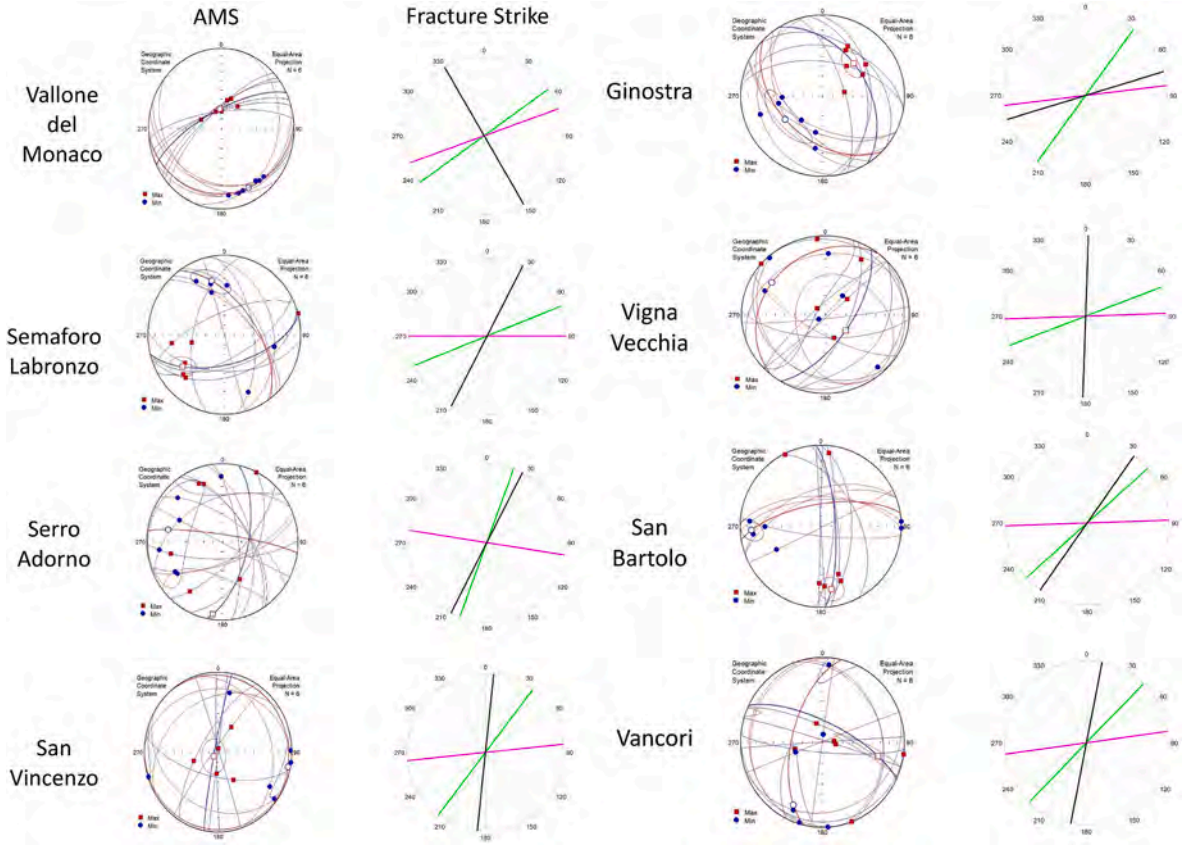

Fig. 12. Comparison of AMS Kmax (left, red) and Kmin (left, blue) with average island fracture strike (right, green line), average block fracture strike (right, magenta line) and average microfracture strike (right, black line) of sampled basalts. (For interpretation of the references to colour in this figure legend, the reader is referred to the Web version of this article.)

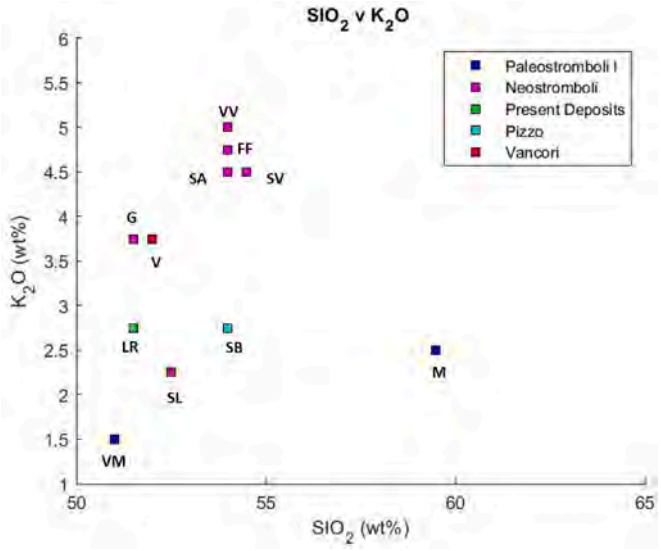

Fig. 13. SIO_2 and K_2O contents of sampled basalts from different lithosomes using data from Francalanci et al., (2013) including: Vallone del Monaco (VM), Malpasso (M), Vancori (V), Serro Adorno (SA), Semaforo Labronzo (SL), San Vincenzo (SV), Ginostra (G) Vigna Vecchia (VV), Filo de Fuoco (FF), San Bartolo and Le Rochette.

observed to increases in Sr and supercritical fluid combined. The increase in volatile content enabled bubble growth in the magma and increased buoyancy limiting fractional crystallisation and the complete crystallisation of minerals such as plagioclase in addition to forming void spaces and cooling microfractures (Fig. 3a, c, 3e, 3g & 3l) leading to a high microscale fracture density (Fig. 11) (Owen et al., 2019). Previous studies have examined that the variations in crystal and asperity content as well as the presence of microfracturing can decrease the structural integrity of basalts (Heap et al., 2016).The influence of these variables has been recorded to increase their porosity thus reducing the P-wave velocity as well material strength and elasticity (Vinciguerra et al., 2005; Di Muro et al., 2021; Heap and Violay, 2021).

5.1. Multiscale P-wave velocity comparisons

A link between fracture density and P-wave velocity can be determined through numerical inversion models that can compare fracture images with laboratory data (Nasseri et al., 2007; Alcock et al., 2023). Thus, a direct multiscale comparison can be established using P-wave velocity. Assuming that fractures are isotropic, numerical inversion models have assessed how fracture damage can affect the elastic properties of rocks. Using equation (6) from Nasseri et al. (2007) fracture density (ρ_c) can be defined as:

$$\rho_c = \frac{1}{V}\sum_{i=1}^{N} c_i^3 \tag{4}$$

where c_i^3 is the radius of the ith crack and N is the total number of cracks in the representative volume V. This definition is then used to calculate the Numerical Youngs Modulus, E^* (Eq. (5)), and from that, the elastic P-wave velocity, v_p (Eq. (6)), via the following two relationships:

$$\frac{E_0}{E^*} = 1 + \frac{16\left(1-a_0^2\right)\left(1-\frac{3a_0}{10}\right)}{9\left(1\frac{a_0}{2}\right)}\rho_c \tag{5}$$

$$v_p = \sqrt{\left(E^* \Big/ \rho\left(\frac{(1-a_0)}{(1-2a_0)(1+a_0)}\right)\right)} \tag{6}$$

where E_0 and a_0 are the directly measured Youngs modulus and Poisson's ratio of the basalts.

Numerically derived elastic P-wave velocity has been calculated using sample fracture density from island and microscopic scales (Table 7) then subsequently compared against laboratory measured P-wave velocity (Fig. 14). Here we observe that in all samples the numerical model replicates the behaviour of the decreasing P-wave velocity with increasing number of microfractures (Castellano et al., 2008; Patanè et al., 2017). P-wave velocity was closely replicated in Vancori, San Bartolo, Le Roccette and Neostromboli basalts for experiments performed in dry or wet conditions. However in the case of minimally fractured rocks such as the Vallone del Monaco basalt, while the numerical estimations are within 0.5 km/s of the measured value this highlights the skewered effect that fracture density can have as an input at both an island and microscale from which the P-wave velocity can be established (Nasseri et al., 2007, 2009). The numerical data gathered estimates the sampled basalts velocity as 2.5 km/s < Vp < 5.5 km/s which is consistent with field scale P-wave tomography models collected from upper 400 m of the edifice that estimated 2.0 km/s < Vp < 6.0 km/s (Castellano et al., 2008; Patanè et al., 2017). Tomographic studies of the edifice have identified that the P-wave velocity would be lower above sea level (Vp < 3.0 km/s) compared to high velocity bodies (Vp > 4.0 km/s) closer to the shallow magma several km's beneath the surface (Patanè et al., 2017). Seismic tomography surveys of the edifice have imaged the inner structure of Stromboli to aid in understanding the evolution of subvolcanic magmatic systems and the geometry of the edifice. High velocity bodies in the edifice are indicative of cumulated old intrusions linked to previous volcanic activity (Castellano et al., 2008; Patanè et al., 2017). Overall, the numerical island and microscale Vp data support tomographic results with numerically derived Vp being near or above 4.0 km/s which is consistent with the identification of old preferential magma pathways. Over time the surface of the edifice has become more fractured due to volcano-tectonic processes and this can be reflected in the low numerical P-wave velocity estimated around the SDF and the along the NE/SW zone of weakness (3.20 Km/s < Vp < 4.60 km/s) which was consistent with Patanè et al. (2017) that estimated P-wave velocity as 3.0 km/s < Vp < 5.0 Km/s whom have examined the P-wave velocity. Low P-wave velocities values (Vp < 3.50 km/s) are indicative of highly fractured materials that have formed the surface of the volcano while high P-wave velocity values (Vp > 3.50 km/s) can be correlated with intrusive high velocity bodies related to historic magma pathways along the zone of weakness that have fed eruptive activity (Winkler and Nur, 1982; Apuani et al., 2005b; Patanè et al., 2017). Numerical P-wave inversion can be used as a tool to evaluate the seismic behaviour of the upper parts of the edifice. By Identifying the seismic behaviour of the upper edifice and being able to relate velocity changes to structural or plumbing system variations is important for monitoring slope instability from intruding magma.

Table 7
Numerically derived P-wave velocity from Island and microscale fracture density.

Sample	Island P-wave Velocity (km/s)	Microscale P-wave Velocity (km/s)
Vallone del Monaco	5.27	3.94
Malpasso	3.87	5.05
Serro Adorno	3.22	3.27
Semaforo Labronzo	4.57	3.41
San Vincenzo	3.82	3.44
Ginostra	3.70	3.73
Vigna Vecchia	4.14	3.74
Le Rochette	3.89	2.80
Filo de Fuoco	3.98	4.50
San Bartolo	3.91	3.61
Vancori	3.59	4.17

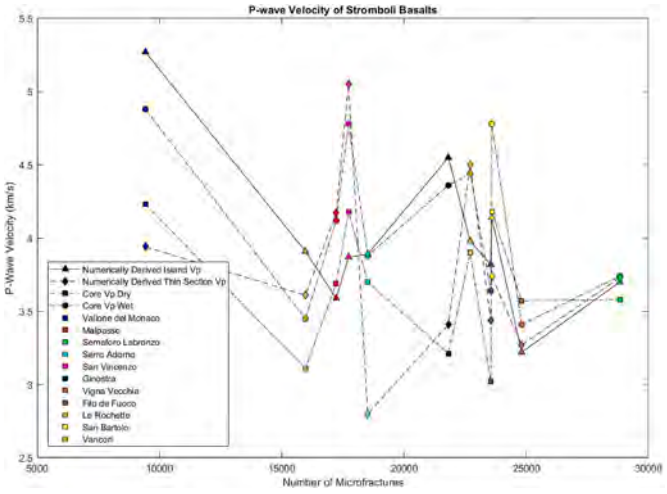

Fig. 14. Comparison of laboratory and numerically derived P-wave velocity using Island and microscale fracture density values.The numerical and measured P-wave velocities have been compared to the number of microfractures to assess the influence of microfracturing on the estimated P-wave vleocity.

5.2. Rock mass strengths

The material characteristics of the sampled basalts were evaluated using the Hoek and Brown failure criterion (Hoek et al., 2002). The mean UCS (σ_{ci}) of samples gathered in this investigation was used as an input value for the failure criterion equation (Eq. (7)).

$$\sigma_1' = \sigma_3' + \sigma_{ci}\left(m_b \frac{\sigma_1'}{\sigma_{ci}} + s\right)^a \tag{7}$$

$$m_b = m_i \exp\left(\frac{GSI - 100}{28 - 14D}\right) \tag{8}$$

Where, m_b is the reduced value of the material constant, and s and a are the rock mass functions of the Geological Strength Index (GSI) and factor of disturbance (D) for each lithotechnical unit as defined in Apuani et al. (2005a). These values were then used to determine the rock mass (σ_{cm}'), cohesive (c') and tensile (σ_t) strengths of the Stromboli basalts (Eqs. (9)–(11)).

$$\sigma_{cm}' = \sigma_{ci} \bullet \left(\frac{(m_b + 4s - a(m_b - 8s))(m_b \div 4 + s)^{a-1}}{2(1+a)(2+a)} + s\right)^a \tag{9}$$

$$c' = \frac{\sigma_{ci}\left[(1+2a)s + (1-a)\, m_b\sigma_{3n}'\right](s + m_b\sigma_{3n}')^{a-1}}{(1+a)(2+a)\sqrt{1 + (6a\, m_b(s + m_b\sigma_{3n}')^{a-1})\Big/((1+a)(2+a))}} \tag{10}$$

$$\sigma_t = \frac{s\sigma_{ci}}{m_b} \tag{11}$$

Where $\sigma_{3n}' = \sigma_{3\,max}'/\sigma_{ci}$. Here we observe that the data collected on the material properties of Stromboli basalts (Table 8) can be compared to previous structural investigations at the Stromboli edifice (Apuani et al., 2005a, 2005b). The material properties of Paleostromboli 1 basalts (Vallone del Monaco & Malpasso) are consistent with the defined lithotechnical Lava unit presented in Apuani et al. (2005a) however,

Table 8
Rock mass properties of Stromboli basalts as determined by Hoek-Brown failure criterion.

Sample	GSI[a]	D[a]	m_i*	m_b*	s[a]	a[a]	σ'_3 (MPa)	σ'_1 (MPa)	σ_t (MPa)	c' (MPa)	σ'_{cm} (MPa)
Vallone del Monaco	40	0	19	2.2	0.0013	0.5	0	2.8	−0.053	3.6	17.1
Malpasso	40	0	19	2.2	0.0013	0.5	0	2.5	−0.047	3.2	15.1
Semaforo Labronzo	30	0	19	1.6	0.0004	0.5	0	0.9	−0.014	1.9	8.1
Serro Adorno	30	0	19	1.6	0.0004	0.5	0	0.4	−0.006	0.8	3.6
San Vincenzo	30	0	19	1.6	0.0004	0.5	0	0.7	−0.011	1.5	6.4
Ginostra	30	0	19	1.6	0.0004	0.5	0	0.8	−0.013	1.8	7.5
Vigna Vecchia	30	0	19	1.6	0.0004	0.5	0	0.7	−0.011	1.4	6.2
Filo de Fuoco	30	0	19	1.6	0.0004	0.5	0	1.2	−0.019	2.5	10.6
Le Rochette	30	0	19	1.6	0.0004	0.5	0	0.9	−0.014	1.9	8.1
San Bartolo	15	0	19	0.7	0.0013	0.6	0	0.9	−0.063	2.6	3.1
Vancori	30	0	19	1.6	0.0004	0.5	0	0.5	−0.009	1.1	4.9

[a] As determined by Apuani et al. (2005a) for each respective lithotechnical unit.

following the magma evolution to the Vancori and Neostromboli the properties of the basalts reflect Breccia and Lava + Breccia respectively.

6. Conclusions

The physical, mechanical and fracture properties around Stromboli volcano (Italy) have been compared at multiple scales to understand how volcano-tectonic processes induced from a prevalent NE/SW regional tectonic regime have influenced fracture development associated with intrusive activity along the NE/SW zone of weakness and around the natural depression of Sciara del Fuoco (SDF). Fracture quantification using the FracPaQ toolbox has been integrated with rock physics experiments and magnetic fabric anisotropy assessments to cross-reference the variation in fracture damage with known areas of collapse.

We conclude that the role of the NE/SW regional system has played a major role in the distribution and orientation of fracturing around the volcanic edifice as terrestrial fractures are aligned to the zone of weakness and concentrated around collapsed zones that have been subject to continuous intrusive activity with quantitative assessments identifying that fracturing was greatest in units that had been subject to major instability.

New insights have been gathered via laboratory assessments conducted on lithological units representative of the evolution of Stromboli basalts within and outside the proposed NE/SW zone of weakness. A lithological dependency between seismic (3.0 km/s < Vp < 4.9 km/s), strength (23.7 MPa < UCS <92.3 MPa), elasticity (4.5 GPa < Ɛ < 11.2 GPa) and porosity changes (2.8 < φ < 23.7) has been found. Quantitative microfracture assessment through petrographic analysis has also identified a lithological dependency in the number of microfractures (9423–28824) and their fracture densities of ($0.004\ \mu m^{-2} < \rho_c < 0.012\ \mu m^{-2}$) with microfractures distribution concentrated along preferential planes of cleavages and/or around asperities.

We further conclude that regional NE/SW zone of weakness can be assessed by examining the properties of macroscopic and microscopic fractures which can be subsequently cross correlated alongside the strikes of lineation and foliation of magnetic fabric while island fracture and microfracture density data can be computed to produce an estimated numerical value for P-wave velocity to simulate seismic behavior at a field scale. The techniques provide a novel method to examine how the NE/SW zone of weakness and areas of collapse can influence fracturing at the different scales of the edifice.

CRediT authorship contribution statement

T. Alcock: Writing – review & editing, Writing – original draft, Methodology, Formal analysis. **S. Vinciguerra:** Writing – review & editing, Writing – original draft, Supervision, Project administration, Investigation, Funding acquisition, Conceptualization. **P.M. Benson:** Validation, Supervision, Software, Methodology, Data curation. **D. Bullen:** Writing – original draft, Supervision, Methodology, Investigation, Data curation.

Declaration of competing interest

The authors declare that they have no known competing financial interests or personal relationships that could have appeared to influence the work reported in this paper.

Data availability

Data will be made available on request.

References

Acocella, V., Tibaldi, A., 2005. Dike propagation driven by volcano collapse: a general model tested at Stromboli, Italy. Geophys. Res. Lett. 32, 1–4. https://doi.org/10.1029/2004GL022248.

Aiuppa, A., Bertagnini, A., Métrich, N., Moretti, R., Di Muro, A., Liuzzo, M., Tamburello, G., 2010. A model of degassing for Stromboli volcano. Earth Planet Sci. Lett. 295, 195–204. https://doi.org/10.1016/j.epsl.2010.03.040.

Alcock, T., Bullen, D., Benson, P.M., Vinciguerra, S., 2023. Temperature-driven microfracturing in granite: the interplay between microstructure, mineralogy and tensile strength. Heliyon 9, e13871. https://doi.org/10.1016/j.heliyon.2023.e13871.

Apuani, T., Corazzato, C., 2009. Numerical model of the Stromboli volcano (Italy) including the effect of magma pressure in the dyke system. Rock Mech. Rock Eng. 42, 53–72. https://doi.org/10.1007/s00603-008-0163-1.

Apuani, T., Corazzato, C., Cancelli, A., Tibaldi, A., 2005a. Stability of a collapsing volcano (Stromboli, Italy): limit equilibrium analysis and numerical modelling. J. Volcanol. Geoth. Res. 144, 191–210. https://doi.org/10.1016/j.jvolgeores.2004.11.028.

Apuani, T., Corazzato, C., Cancelli, A., Tibaldi, A., 2005b. Physical and mechanical properties of rock masses at Stromboli: a dataset for volcano instability evaluation. Bull. Eng. Geol. Environ. 64, 419–431. https://doi.org/10.1007/s10064-005-0007-0.

Bai, L., Baker, D.R., Rivers, M., 2008. Experimental study of bubble growth in Stromboli basalt melts at 1 atm. Earth Planet Sci. Lett. 267, 533–547. https://doi.org/10.1016/j.epsl.2007.11.063.

Bertagnini, A., Métrich, N., Landi, P., Rosi, M., 2003. Stromboli volcano (Aeolian Archipelago, Italy): an open window on the deep-feeding system of a steady state basaltic volcano. J. Geophys. Res. Solid Earth 108. https://doi.org/10.1029/2002jb002146.

Bhowmick, S., Kumar Mondal, T., 2020. Control of pre-existing fabric in fracture formation, reactivation and vein emplacement under variable fluid pressure conditions: an example from Archean greenstone belt, India. Solid Earth 11, 1227–1246. https://doi.org/10.5194/se-11-1227-2020.

Borradaile, G.J., Hamilton, T., 2004. Magnetic fabrics may proxy as neotectonic stress trajectories, Polis rift, Cyprus. Tectonics 23, 1–11. https://doi.org/10.1029/2002TC001434.

Bubeck, A., Walker, R.J., Healy, D., Dobbs, M., Holwell, D.A., 2017. Pore geometry as a control on rock strength. Earth Planet Sci. Lett. 457, 38–48.

Castellano, M., Augusti, V., De Cesare, W., Favali, P., Frugoni, F., Montuori, C., Sgroi, T., P, D.G., Govoni, A., Moretti, M., Patane, D., Cocina, O., Zuccarello, L., Marsella, E., Aiello, G., Di Fiore, V., Ligi, M., Bortoluzzi, G., Ferrante, V., Marchetti, E., Lacanna, G., Uliver, G., 2008. Seismic tomography experiment at Italy ' s Stromboli volcano. Eos 89, 20–23. https://doi.org/10.1029/2002JB001919.

Corazzato, C., Francalanci, L., Menna, M., Petrone, C.M., Renzulli, A., Tibaldi, A., Vezzoli, L., 2008. What controls sheet intrusion in volcanoes? Structure and petrology of the Stromboli sheet complex, Italy. J. Volcanol. Geoth. Res. 173, 26–54. https://doi.org/10.1016/j.jvolgeores.2008.01.006.

del Moro, S., Renzulli, A., Tribaudino, M., 2011. Pyrometamorphic processes at the magma-hydrothermal system interface of active volcanoes: evidence from buchite ejecta of Stromboli (Aeolian Islands, Italy). J. Petrol. 52, 541–564. https://doi.org/10.1093/petrology/egq090.

del Potro, R., Hürlimann, M., 2009. The decrease in the shear strength of volcanic materials with argillic hydrothermal alteration, insights from the summit region of Teide stratovolcano, Tenerife. Eng. Geol. 104, 135–143. https://doi.org/10.1016/j.enggeo.2008.09.005.

Di Muro, A., Schwarzlmueller, F., Kueppers, U., Heap, M., Dingwell, D.B., 2021. Petrophysical characterisation of volcanic ejecta to constrain subsurface lithological heterogeneities: implications for edifice stability at basaltic volcanoes. Volcanica 4, 41–66. https://doi.org/10.30909/VOL.04.01.4166.

Di Stefano, F., Mollo, S., Ubide, T., Petrone, C.M., Caulfield, J., Scarlato, P., Nazzari, M., Andronico, D., Del Bello, E., 2020. Mush cannibalism and disruption recorded by clinopyroxene phenocrysts at Stromboli volcano: new insights from recent 2003–2017 activity. Lithos 360–361. https://doi.org/10.1016/j.lithos.2020.105440.

Di Traglia, F., Bartolini, S., Artesi, E., Nolesini, T., Ciampalini, A., Lagomarsino, D., Martí, J., Casagli, N., 2018. Susceptibility of intrusion-related landslides at volcanic islands: the Stromboli case study. Landslides 15, 21–29. https://doi.org/10.1007/s10346-017-0866-z.

Di Traglia, F., De Luca, C., Fornaciai, A., Manzo, M., Nolesini, T., Favalli, M., Lanari, R., Casagli, N., Casu, F., 2021. Remote sensing of steep-slope volcanoes: the Stromboli case studyEGU General Assembly, online, 19-21 April 2021, EGU21-90539. https://doi.org/10.5194/egusphere-egu21-9539.

Edmonds, M., Aiuppa, A., Humphreys, M., Moretti, R., Giudice, G., Martin, R.S., Herd, R. A., Christopher, T., 2010. Excess volatiles supplied by mingling of mafic magma at an andesite arc volcano. G-cubed 11, 1–16. https://doi.org/10.1029/2009GC002781.

Falsaperla, S., Lanzafame, G., Longo, V., Spampinato, S., 1999. Regional stress field in the area of Stromboli (Italy): insights into structural data and crustal tectonic earthquakes. J. Volcanol. Geoth. Res. 88, 147–166. https://doi.org/10.1016/S0377-0273(98)00113-9.

Finizola, A., Sortino, F., Lénat, J.F., Aubert, M., Ripepe, M., Valenza, M., 2003. The summit hydrothermal system of Stromboli. New insights from self-potential, temperature, CO2 and fumarolic fluid measurements, with structural and monitoring implications. Bull. Volcanol. 65, 486–504. https://doi.org/10.1007/s00445-003-0276-z.

Fisher, R., Schmincke, H.U., 1984. Pyroclastic Flow Deposits. Pyroclastic Rocks, pp. 186–230.

Francalanci, L., Lucchi, F., Keller, J., De Astis, G., Tranne, C.A., 2013. Chapter 13 Eruptive, volcano-tectonic and magmatic history of the Stromboli volcano (north-eastern Aeolian archipelago). Geological Society, London, Memoirs 37, 397–471. https://doi.org/10.1144/m37.13.

Healy, D., Rizzo, R.E., Cornwell, D.G., Farrell, N.J.C., Watkins, H., Timms, N.E., Gomez-Rivas, E., Smith, M., 2017. FracPaQ: a MATLAB™ toolbox for the quantification of fracture patterns. J. Struct. Geol. 95, 1–16. https://doi.org/10.1016/j.jsg.2016.12.003.

Heap, M.J., Baumann, T., Gilg, H.A., Kolzenburg, S., Ryan, A.G., Villeneuve, M., Russell, J.K., Kennedy, L.A., Rosas-Carbajal, M., Clynne, M.A., 2021a. Hydrothermal alteration can result in pore pressurization and volcano instability. Geology 49, 1348–1352. https://doi.org/10.1130/G49063.1.

Heap, M.J., Baumann, T., Rosas-Carbajal, M., Komorowski, J.-C., Gilg, H.A., Villeneuve, M., Moretti, R., Baud, P., Carbillet, L., Harnett, C.E., Reuschlé, T., 2021b. Alteration-Induced Volcano Instability at La Soufri re de Guadeloupe Eastern Caribbean. Solid Earth 126. https://doi.org/10.1029/2021JB022514.

Heap, M.J., Faulkner, D.R., Meredith, P.G., Vinciguerra, S., 2010. Elastic moduli evolution and accompanying stress changes with increasing crack damage: implications for stress changes around fault zones and volcanoes during deformation. Geophys. J. Int. 183, 225–236. https://doi.org/10.1111/j.1365-246X.2010.04726.x.

Heap, M.J., Villeneuve, M., Albino, F., Farquharson, J.I., Brothelande, E., Amelung, F., Got, J.L., Baud, P., 2020b. Towards more realistic values of elastic moduli for volcano modelling. J. Volcanol. Geoth. Res. https://doi.org/10.1016/j.jvolgeores.2019.106684.

Heap, M.J., Vinciguerra, S., Meredith, P.G., 2009. The evolution of elastic moduli with increasing crack damage during cyclic stressing of a basalt from Mt. Etna volcano. Tectonophysics 471, 153–160. https://doi.org/10.1016/j.tecto.2008.10.004.

Heap, M.J., Violay, M.E.S., 2021. The mechanical behaviour and failure modes of volcanic rocks: a review. Bull. Volcanol. 83 https://doi.org/10.1007/s00445-021-01447-2.

Heap, M.J., Wadsworth, F.B., Xu, T., Chen, C. feng, Tang, C., 2016. The strength of heterogeneous volcanic rocks: a 2D approximation. J. Volcanol. Geoth. Res. 319, 1–11. https://doi.org/10.1016/j.jvolgeores.2016.03.013.

Heap, M.J., Xu, T., Chen, C. feng, 2014. The influence of porosity and vesicle size on the brittle strength of volcanic rocks and magma. Bull. Volcanol. 76, 1–15. https://doi.org/10.1007/s00445-014-0856-0.

Hildenbrand, A., Gillot, P.Y., Le Roy, I., 2004. Volcano-tectonic and geochemical evolution of an oceanic intra-plate volcano: tahiti-Nui (French Polynesia). Earth Planet Sci. Lett. 217, 349–365. https://doi.org/10.1016/S0012-821X(03)00599-5.

Hoek, E., Carranza-Torres, C., Corkburn, B., 2002. HOEK-BROWN failure criterion. Proceedings of NARMS-Tac 1 (1), 267–273. https://doi.org/10.1016/0148-9062(74)91782-3.

Hora, J.M., Singer, B.S., Wörner, G., 2007. Volcano evolution and eruptive flux on the thick crust of the andean central volcanic zone: 40Ar/39Ar constraints from volcán parinacota, Chile. Bull. Geol. Soc. Am. 119 (1), 343–362. https://doi.org/10.1130/B25954.

Intrieri, E., Di Traglia, F., Del Ventisette, C., Gigli, G., Mugnai, F., Luzi, G., Casagli, N., 2013. Flank instability of Stromboli volcano (aeolian islands, southern Italy): integration of GB-InSAR and geomorphological observations. Geomorphology 201, 60–69. https://doi.org/10.1016/j.geomorph.2013.06.007.

Karaman, K., Kesimal, A., 2015. Evaluation of the influence of porosity on the engineering properties of volcanic rocks from the Eastern Black Sea Region: NE Turkey. Arabian J. Geosci. 8, 557–564. https://doi.org/10.1007/s12517-013-1217-6.

Lu, R.K., Zhang, G.W., Zhong, H.M., Xia, J., Tong, J.S., Yu, X.J., 2008. Characteristics of magnetic fabrics in western segment of the Altun fault belt and its tectonic significance. Acta Geophysica Sinica 51, 752–761. https://doi.org/10.1002/cjg2.1244.

Lucchi, F., 2019. On the use of unconformities in volcanic stratigraphy and mapping: insights from the Aeolian Islands (southern Italy). J. Volcanol. Geoth. Res. 1–23. https://doi.org/10.1016/j.jvolgeores.2019.01.014.

Manconi, A., Longpe, M.A., Walter, T.R., Troll, V.R., Hansteen, T.H., 2009. The effects of flank collapses on volcano plumbing systems. Geology 37 (1), 1099–1102. https://doi.org/10.1130/G30104A.

Mauldon, M., Dunne, W.M., Rohrbaugh, M.B., 2001. Circular scanlines and circular windows: new tools for characterizing the geometry of fracture traces. J. Struct. Geol. 23, 247–258. https://doi.org/10.1016/S0191-8141(00)00094-8.

Nasseri, M.H.B., Schubnel, A., Young, R.P., 2007. Coupled evolutions of fracture toughness and elastic wave velocities at high crack density in thermally treated. Westerly granite 44, 601–616. https://doi.org/10.1016/j.ijrmms.2006.09.008.

Nasseri, M.H.B., Tatone, B.S.A., Grasselli, G., Young, R.P., 2009. Fracture toughness and fracture roughness interrelationship in thermally treated westerly granite. Pure Appl. Geophys. 166, 801–822. https://doi.org/10.1007/s00024-009-0476-3.

Owen, J., Shea, T., Tuffen, H., 2019. Basalt, unveiling fluid-filled fractures, inducing sediment intra-void transport, ephemerally: examples from katla 1918. J. Volcanol. Geoth. Res. 369, 121–144. https://doi.org/10.1016/j.jvolgeores.2018.11.002.

Palaseanu-Lovejoy, M., Bisson, M., Spinetti, C., Buongiorno, M.F., Alexandrov, O., Cecere, T., 2019. High-resolution and accurate topography reconstruction of Mount Etna from pleiades satellite data. Rem. Sens. 11, 1–17. https://doi.org/10.3390/rs11242983.

Patanè, D., Barberi, G., De Gori, P., Cocina, O., Zuccarello, L., Garcia-Yeguas, A., Castellano, M., D'Alessandro, A., Sgroi, T., 2017. The shallow magma chamber of Stromboli Volcano (Italy). Geophys. Res. Lett. 44, 6589–6596. https://doi.org/10.1002/2017GL073008.

Petrone, C.M., Mollo, S., Gertisser, R., Buret, Y., Scarlato, P., Del Bello, E., Andronico, D., Ellis, B., Pontesilli, A., De Astis, G., Giacomoni, P.P., Coltorti, M., Reagan, M., 2022. Magma recharge and mush rejuvenation drive paroxysmal activity at Stromboli volcano. Nat. Commun. 13, 1–17. https://doi.org/10.1038/s41467-022-35405-z.

Petrone, C.M., Olmi, F., Braschi, E., Francalanci, L., 2006. Mineral chemistry profile: a valuable approach to unravel magma mixing processes in the recent volcanic activity of Stromboli, Italy. Period. Mineral. 75, 277–292.

Pinel, V., Jaupart, C., 2005. Some consequences of volcanic edifice destruction for eruption conditions. J. Volcanol. Geoth. Res. 145, 68–80. https://doi.org/10.1016/j.jvolgeores.2005.01.012.

Pola, A., Crosta, G.B., Fusi, N., Castellanza, R., 2014. General characterization of the mechanical behaviour of different volcanic rocks with respect to alteration. Eng. Geol. 169, 1–13. https://doi.org/10.1016/j.enggeo.2013.11.011.

Reid, M.E., Keith, T.E.C., Kayen, R.E., Iverson, N.R., Iverson, R.M., Brien, D.L., 2010. Volcano collapse promoted by progressive strength reduction: new data from Mount St. Helens. Bull. Volcanol. 72, 761–766. https://doi.org/10.1007/s00445-010-0377-4.

Rossi, S., Petrelli, M., Morgavi, D., Vetere, F.P., Almeev, R.R., Astbury, R.L., Perugini, D., 2019. Role of magma mixing in the pre-eruptive dynamics of the aeolian islands volcanoes (southern tyrrhenian sea, Italy). Lithos 324–325, 165–179. https://doi.org/10.1016/j.lithos.2018.11.004.

Shevchenko, A.V., Dvigalo, V.N., Zorn, E.U., Vassileva, M.S., Massimetti, F., Walter, T.R., Svirid, I.Y., Chirkov, S.A., Ozerov, A.Y., Tsvetkov, V.A., Borisov, I.A., 2021. Constructive and destructive processes during the 2018–2019 eruption episode at Shiveluch volcano, kamchatka, studied from satellite and aerial data. Front. Earth Sci. 9, 1–27. https://doi.org/10.3389/feart.2021.680051.

Simmons, G., Brace, W.F., 1965. Comparison of static and dynamic measurements of compressibility of rocks. J. Geophys. Res. 70, 5649–5656.

Swanson, D., Duffield, W., Fiske, R., 1976. Displacement of the south flank of Kilauea volcano: the result of forceful intrusion of magma into the rift zones. US Geological Survey Professional Paper 963, 37–39. https://doi.org/10.3133/pp963.

Tibaldi, A., 2003. Influence of cone morphology on dykes, Stromboli, Italy. J. Volcanol. Geoth. Res. 126, 79–95. https://doi.org/10.1016/S0377-0273(03)00118-5.

Tibaldi, A., 1996. Mutual influence of dyking and collapses at Stromboli volcano, Italy. Geol. Soc. Spec. Publ. 110, 55–63. https://doi.org/10.1144/GSL.SP.1996.110.01.04.

Tibaldi, A., Bonali, F.L., Corazzato, C., 2014. The diverging volcanic rift system. Tectonophysics 611, 94–113. https://doi.org/10.1016/j.tecto.2013.11.023.

Tibaldi, A., Corazzato, C., 2009. Tectonic and volcanic activity along the Stromboli rift zone and the reciprocal influence on lateral collapses : subaerial and submarine data. Tectnophysics 469, 112–136.

Tibaldi, A., Corazzato, C., Apuani, T., Cancelli, A., 2003. Deformation at Stromboli volcano (Italy) revealed by rock mechanics and structural geology. Tectonophysics 361, 187–204. https://doi.org/10.1016/S0040-1951(02)00589-9.

Tibaldi, A., Corazzato, C., Marani, M., Gamberi, F., 2009. Subaerial-submarine evidence of structures feeding magma to Stromboli Volcano, Italy, and relations with edifice flank failure and creep. Tectonophysics 469, 112–136. https://doi.org/10.1016/j.tecto.2009.01.031.

Vaggelli, G., Francalanci, L., Ruggieri, G., Testi, S., 2003. Persistent polybaric rests of calc-alkaline magmas at Stromboli volcano, Italy: pressure data from fluid inclusions in restitic quartzite nodules. Bull. Volcanol. 65, 385–404. https://doi.org/10.1007/s00445-002-0264-8.

Vinciguerra, S., Trovato, C., Meredith, P.G., Benson, P.M., 2005. Relating seismic velocities , thermal cracking and permeability in. Mt . Etna and Iceland basalts. 42, 900–910. https://doi.org/10.1016/j.ijrmms.2005.05.022.

Voight, B., Elsworth, D., 1997. Failure of volcano slopes. Geotechnique 47.

White, R.S., Drew, J., Martens, H.R., Key, J., Soosalu, H., Jakobsdóttir, S.S., 2011. Dynamics of dyke intrusion in the mid-crust of Iceland. Earth Planet Sci. Lett. 304, 300–312. https://doi.org/10.1016/j.epsl.2011.02.038.

Winkler, K.W., Nur, A., 1982. Seismic attenuation: effects of pore fluids and frictional sliding. Geophysics 47, 1–15. https://doi.org/10.1190/1.1441276.

Zhu, W., Baud, P., Vinciguerra, S., Wong, T. fong, 2016. Micromechanics of brittle faulting and cataclastic flow in Mount Etna basalt. AGU: J. Geophys. Res. Solid Earth 121, 4268–4289. https://doi.org/10.1002/2016JB012826. Received.